

1 **New insights into the vertical structure of the September 2015**
2 **dust storm employing 8 ceilometers and auxiliary measurements**
3 **over Israel**

4

5 Leenes Uzan^{1,2}, Smadar Egert¹, Pinhas Alpert¹

6

7 ¹Department of Geosciences, Raymond and Beverly Sackler Faculty of Exact Sciences,
8 Tel-Aviv University, Tel Aviv, 6997801, Israel.

9 ²The Israeli Meteorological Service, Beit Dagan, Israel.

10

11 Correspondence to: Leenes Uzan (Leenesu@gmail.com)

12

13

14

15

16

17

18

19

20

21

22

23

24

25

26

27

28

29

30

31

32

33

34

35

36 **Abstract**

37

38 On 7 September 2015 an unprecedented and unexceptional extreme dust storm struck the Eastern
39 Mediterranean (EM) basin. Here, we provide an overview of the previous studies and describe the dust
40 plume evolution over a relatively small area, i.e., Israel. This study presents vertical profiles provided by
41 an array of 8 ceilometers covering Israeli shore, inland and mountain regions. We employ multiple tools
42 including spectral radiometers (AERONET), ground particulate matter concentrations, satellite images,
43 global/diffuse/direct solar radiation measurements and radiosonde profiles. Main findings reveal that the
44 dust plume penetrated Israel on the 7 September from the northeast in a downward motion to southwest.
45 On 8 September, the lower level of the dust plume reached 200 m above ground level, generating aerosol
46 optical depth (AOD) above 3, and extreme ground particulate matter concentrations up to $\sim 10,000 \mu\text{m}^{-3}$.
47 A most interesting feature on 8 September was the very high variability in the surface solar radiation
48 in the range of 200-600 W m^{-2} (22 sites) over just a distance of several hundred km in spite of the thick
49 dust layer above. Furthermore, 8 September shows the lowest radiation levels for this event. On the
50 following day, the surface solar radiation increased, thus enabling a late (between 11-12 UTC) sea breeze
51 development mainly in the coastal zone associated with a creation of a narrow dust layer detached from
52 the ground. On 10 September the AOD values started to drop down to ~ 1.5 , the surface concentrations
53 of particulate matter decreased as well as the ceilometers aerosol indications (signal counts) although
54 CALIPSO revealed an upper dust layer remained.

55

56

57

58

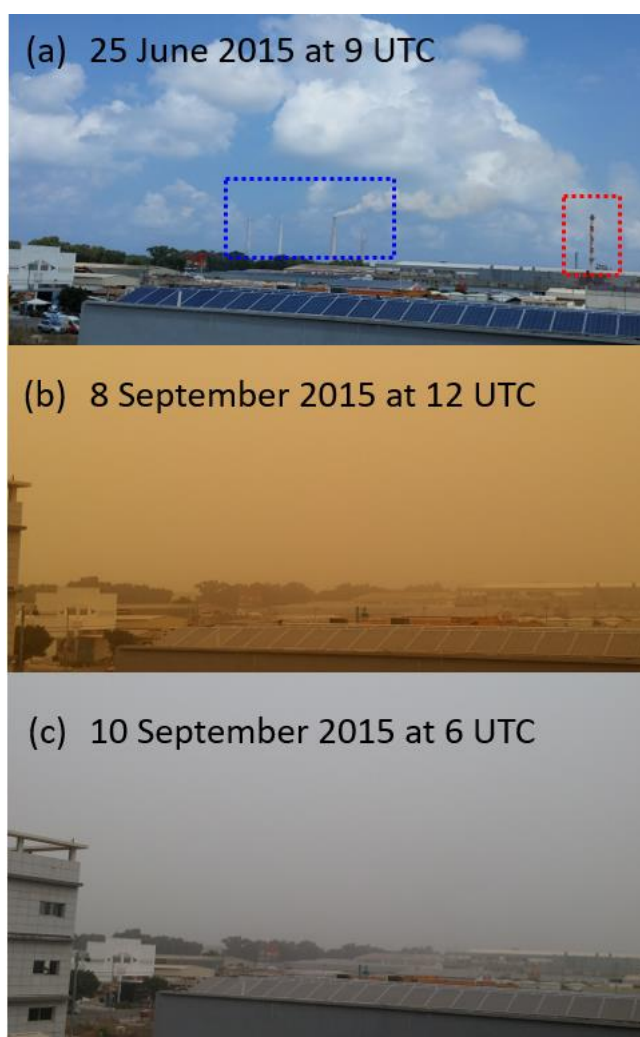
59 **1. Introduction**

60

61 An exceptionally extreme dust storm prevailed over the Eastern Mediterranean (EM) on September
62 2015. The Israeli meteorological service (IMS) declared the dust storm to be extraordinary as it occurred
63 on early September (7-10 September), extended over a time span of 100 hours creating extreme ground
64 level particulate matter (PM) concentrations (e.g. 100 times above the hourly average of PM10 in
65 Jerusalem). On 7 September, prior to the penetration of the dust storm over Israel, IMS reported
66 (<http://www.ims.gov.il/IMS/CLIMATE>; in Hebrew) a heat wave over Israel causing harsh weather
67 conditions of 80-90% relative humidity, 42 °C in valleys, 38 °C in mountains. On 8 September, visibility
68 decreased below 3 km and consequently, inland aviation was prohibited until 9 September (Fig.1).

69 Concurrently, severe ground level PM concentrations resulted with a public warning from outdoor
70 activities issued by the environmental protection ministry. Finally, on 11 September, as visibility
71 increased, the IMS confirmed the dust storm ended, whereas the heat wave was over two days later, on
72 13 September, subsequent to a profound change in weather conditions. The PM concentrations declined
73 to values measured prior to the dust storm (<http://www.svivaaqm.net/Default.rtl.aspx>; in Hebrew) only
74 on 14 September, though the AERONET measurements (<https://aeronet.gsfc.nasa.gov>) stationed in
75 central and southern Israel reveal that the aerosol optical depth (AOD) resumed to values prior to the dust
76 storm only on 17 September.

77
78

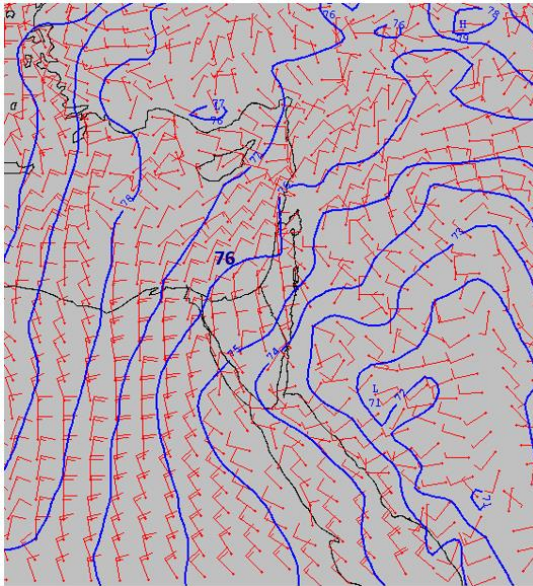


79
80 Figure 1. Photographs taken from the central coast of Israel, adjacent to the Hadera ceilometer, 3.5
81 km southeast to stacks of a power plant (indicated by a blue rectangle) and 600 m north to a factory
82 stack (indicated by a red rectangle). The photographs were taken prior to the dust storm, on 25 July
83 2015 (a), and during the dust storm, on 8 September 2015 (b) and 10 September 2015 (c). Notice that
84 the stacks that are visible on a clear day (a) are invisible during the dust storm (b, c).

85 Investigation of the mechanisms leading the severe dust storm was performed by Gasch et al. (2017)
86 using a state of the art dust transport model ICOSahedral Nonhydrostatic (ICON) with the Aerosol and
87 Reactive Trace gases (ART) (Rieger, et al., 2015). The model concentrated on the EM with one global
88 domain (40 km grid spacing, and 90 vertical levels from 20 m to 75 km) and 4 nested grids (20, 10, 5
89 and 2.5 km grid spacing and 60 vertical levels from 20 m to 22.5 km). Simulations were done for three
90 consecutive days from 6-8 September. Model results delineated an unusual early incidence of an active
91 Red Sea Trough (Fig.2; Alpert et al, 2004) over Mesopotamia, followed by meso-scale convective
92 systems over the Syrian-Iraqi border generating three cold-pool outflows. On the night between 5 and 6
93 September, a convective system fueled by an inflow along the eastern side of the Red Sea Trough, moved
94 northeast over the Turkish-Syrian border region. The convective system intensified overnight and
95 generated a first weak cold pool outflow on 6 September. After sun rise, an increase of surface wind
96 speeds caused dust pick up over Syria. The atmospheric instability over the Syrian-Iraqi border created
97 a second convective cold pool outflow from the Zagros mountain range west into Syria. The gust from
98 the second cold pool outflow ignited a third cold pool outflow at 20 UTC which moved southerly along
99 the eastern flank of the Red Sea Trough. On 7 September 10 UTC, rainfall and an increase of surface
100 wind speeds north-west of Syria strengthened the third cold pool outflow leading to transportation of
101 enormous dust emissions (up to 5 km) southwest. By nightfall of 7 September, the aged second cold pool
102 outflow merged with the third cold pool outflow, over Jordan and southwestern Syria. After midnight,
103 between 7 and 8 September, the dust transported over Israel. Model simulations were compared to in-
104 situ measurements and satellite images: visible electromagnetic spectrum from Moderate Resolution
105 Imaging Spectroradiometer (MODIS: <https://modis.gsfc.nasa.gov/>) aboard the Aqua satellite; AOD from
106 the Terra satellite; RGB dust product from the Spinning Enhanced Visible and InfraRed Imager (SEVIRI)
107 upon the Meteosat Second Generation (MSG) satellite; Total attenuated backscatter from Cloud-Aerosol
108 Lidar upon the Infrared Pathfinder Satellite Observations (CALIPSO: [https://www-
109 calipso.larc.nasa.gov/](https://www-calipso.larc.nasa.gov/)). Investigation over Israel employed measurements from ground level
110 meteorological stations (3 sites) and PM measurements (3 sites). Results revealed the model lacked
111 sufficient development of a super critical flow, which in effect produced the excessive surface wind
112 speeds. Eventually, this misled the forecast of the dust advection southwest into Israel.

113

114



115

116

117

118

119

120

121

122

123

124

125

126

127

128

129

130

131

132

133

134

135

136

137

138

Figure 2. 925 mb map from 7 September 2015 12 UTC of geopotential height of 1 dm interval (blue lines, the 76 dm line is passing over Israel) and wind (red arrows, 10 KT each line). Source: IMS from UKMO British Met Office model.

The fact that forecast models did not succeed in predicting this outstanding dust event motivated Mamouri et al. (2016) to study its origin and development. Their research presented dust load observations in the Cyprus region. Luckily, at the time of the dust storm, an EARLINET (European Aerosol Research lidar Network: <https://www.earlinet.org/>) Raman lidar stationed in Limassol provided vertical dust profiles and valuable optical dust properties of backscatter, extinction, lidar ratio and linear depolarization ratio. They analyzed the optical thickness (AOT) and Angström exponent derived from the MODIS Aqua satellite. MODIS Aqua AOT measurements were compared to the Limassol lidar observations, AOD measurements from two AERONET sites (Cyprus and Israel) and ground level PM10 concentration from four Cyprus sites. On 7 September, EARLINET lidar observations measured two dust layers (extending up to 1.7 km ASL and between 1.7-3.5 km ASL). The dust particle extinction coefficient measured in Limassol had reached 1000 Mm^{-1} followed by high PM10 concentration of $2000 \mu\text{m m}^{-3}$. Extreme values over Limassol, were reported on 8 September as MODIS Aqua AOT observations exceeded 5 (assuming overestimation up to 1.5) and hourly PM10 concentration of about $8,000 \mu\text{m m}^{-3}$ (with uncertainties in the order of 50%). Unfortunately, on 8 September, the lidar was intentionally shut down to avoid potential damage to the instrument. Lidar observations indicated another dense dust outbreak (1-3 km ASL) reaching Limassol on 10 September, also visible by AOT MODIS Aqua. The researchers concluded the scale of the dust storm features was too small for global and regional dust transport models. They presumed that the initiation of the dust plume was due to an intense dust

139 storm (haboob) in northeastern Syria and northern Iraq, leading to vigorous downbursts which
140 consequently pushed huge amounts of dust and sand to the atmosphere. The lidar observations indicated
141 a double layer structure of the dust, 1.5 and 4 km ASL, pointing to multiple dust sources.

142
143 Solomos et al., (2016) continued the investigation of the formation and mechanism of the dust storm
144 over Cyprus by a high regional atmospheric model of the integrated community limited area modeling
145 system (RAMS-ICLAMS). The model simulations focused on the generation of the dust storm on 6 and
146 7 September. Model results were fine-tuned by observations from EARLINET lidar stationed in
147 Limassol, radiosonde data from five sites (Cyprus, Israel, Jordan, and two from Turkey) and satellite
148 imagery from MSG SEVIRI and CALIPSO CALIOP. The model was set to three grid space domains:
149 an external grid of 12X12 km, (over the EM) an inner set at 4X4 km (over northern EM) and 2X2 km
150 grid for cloud resolving (over northeastern Syria). The vertical structure consisted of 50 terrain following
151 levels up to 18 km. The researchers estimated a strong thermal low over Syria was followed by
152 convection activity over the Iraq-Iran-Syria-Turkey borderline. Combined with land use changes
153 (aftermath of the war held in Syria), these conditions manufactured the extreme dust storm. The model
154 succeeded to describe the dust westward flow of a haboob containing the dust previously elevated over
155 Syria also observed by MSG SEVIRI and EARLINET lidar. However, there were some inaccuracies in
156 the quantification of dust mass profiles. The researchers attributed the model discrepancies to the limited
157 ability of the model to properly resolve dust and atmospheric properties (e.g. change of land use and
158 intense downward mixing).

159
160 Pu and Ginoux, (2016) examined the connection between the natural climate variability (the
161 Pacific decadal oscillation) and the dust optical depth (DOD) in Syria between the years 2003-2015.
162 DODs were derived by the deep blue algorithm (Hsu et al., 2013) aerosol product from MODIS Terra
163 and MODIS Aqua satellite (10 km resolution). AODs were estimated by the European Centre for
164 Medium-Range Weather Forecasts (ECMWF) reanalysis model (horizontal resolution of 80 km and 37
165 vertical levels) and produced by the Geophysical Fluid Dynamics Laboratory (GFDL) Atmospheric
166 model (AM3) (Donner et al., 2011). In addition, the AM3 model produced mass distribution and optical
167 properties of aerosols, their chemical production, transport, and dry or wet deposition. Comparison of
168 the model AODs, AERONET AOD measurements and DODs from satellite observations revealed the
169 model underestimated the AODs particularly in the EM. The authors assumed that the soil moisture
170 parameter in the model were not set properly resulting in the AOD dissimilarities.

171

172 The impact of the conflict in Syria on the aridity of the region and therefore, a possible direct
173 impact on the generation of the September dust storm was examined by Parolari et al., (2016). The
174 researchers conducted simulations using the Advanced Research Weather Research and Forecasting
175 (WRF-ARW) model from 30 August 2015 to 10 September 2015 over the EM. The model consisted of
176 two nested domains (9 and 3 km grid spacing and 35 vertical levels). Daily and monthly AOD data from
177 MODIS were computed by the deep blue algorithm over land. The monthly average of September 2015
178 vegetation status in the region was estimated by MODIS normalized difference vegetation index (NDVI).
179 Historical data was divided into two periods: none-drought (2001-2006) and drought (2007-2010). Wind
180 shear stress was calculated to estimate wind erosion. Main findings reveal that the enhanced dust uplift
181 and transportation of the September 2015 dust storm was due to meteorological conditions rather than
182 the land-use changes attributed to the civil conflict in Syria. WRF simulations revealed northwesterly
183 winds west of the low pressure zone in the Syrian-Iraqi border were associated with dust storms in the
184 Middle East (Rao et al., 2003). The source of elevated dust concentrations over the EM coast on 7 and 8
185 September were attributed to the cyclone front movement. On 6 September low level winds (700 hPa)
186 were opposite to the northwesterly high level winds (300 hPa), consequently generating enhanced surface
187 shear stress and transported re-suspended PM westward. Furthermore, based on the past 20 years, the
188 Israeli summer of 2015 was unusually dry and hot and therefore enabled easier updraft of dust soil
189 increasing the probability of dust emissions.

190
191 Jasmin (2016) compared the dust plume aerosol content provided by MSG SEVIRI observations,
192 to the generation of the dust storm produced by the open source Meteoinfo model (Wang, 2014). The
193 Meteoinfo model was based on meteorological variables from ECMWF. The model revealed a formation
194 of two simultaneous dust storms, from northern Syria and the Egyptian Sinai desert, as a result of updrafts
195 created by low pressure systems.

196
197 The aforementioned studies (summarized in Table 1) focused on the generation of the dust storm
198 in the Syria region based on transport models, satellite imagery and in situ measurements. In our study
199 we focus on the evolution of the dust plume over Israel in the lower atmosphere based on an array of 8
200 ceilometers and auxiliary instruments described in Sect. 2. The list of instruments includes; ceilometers,
201 PM measurements, AERONET, radiosonde, solar radiation and satellite imagery. Sect. 3 presents the
202 delineation of the dust plume spatial and temporal scheme from 7 - 10 September 2015. We discuss and
203 compare the results between the different measurements. Conclusions and main findings of the dust
204 plume progress in the lower atmosphere are given in Sect. 4.

205

2. Instruments

2.1 Ceilometers

Lidars are widely used for aerosol studies (Ansmann et al., 2011; Papayannis et al., 2008) including desert dust characteristics and transport process (Mona et al., 2012). Ceilometers, initially intended for cloud level height detection, are automatic low cost lidars widespread in airports and weather stations worldwide. As single wavelength lidars, ceilometers cannot produce the information aerosol properties such as size distribution, scattering and absorption coefficients. Nevertheless, with improvement of hardware and firmware over the years, ceilometers have become a valuable tool in the study of the atmospheric boundary layer and the vertical distribution of aerosols layers (Haeffelin and Angelini, 2012; Ansmann et al., 2003). Furthermore, in 2013 ceilometers were assimilated in the EUMETNET (European Meteorological Services network) profiling program across Europe (<http://eumetnet.eu/activities/observations-programme/current-activities/e-profile/alc-network/>). The main research tool in this study is the Vaisala ceilometers type CL31, commonly deployed worldwide.

CL31 is a pulsed elastic micro lidar, employing an Indium Gallium Arsenide (InGaAs) laser diode transmitter of near infrared wavelength (910 nm \pm 10 nm at 25°C). In order to compensate the low pulse energy of the laser (hence defined "eye-safe") and to provide sufficient signal to noise ratio, the pulse repetition rate is of 10 kHz (Vaisala ceilometer CL31 user's guide: <http://www.vaisala.com>). The backscatter signals are collected by an avalanche photodiode (APD) receiver and designed into range corrected signal profiles within a reporting interval of 2-120 s (determined by the user) given in relative unites (signal counts). The ceilometer profiles are automatically corrected by a cosmetic shift of the backscatter signal (to better visualize the clouds base), an obstruction correction (when the ceilometers' window is blocked by a local obstacle) and an overlap correction (to the height where the receiver field of view reaches complete overlap with the emitted laser beam).

Vaisala provides a scaling factor transferring signal counts to attenuated backscatter units by a multiplication factor of 10^{-8} . The scaling factor was obtained using a calibration procedure operated on a several instruments and cross-checked by signal integral from water clouds. The uncertainty of calibrated attenuated backscatter profile (with a 100% clean window condition) was of ± 10 %. The uncertainty for the estimated attenuated backscatter was of ± 20 % (Münkel C., private communication). However, Kotthaus et al., (2016) emphasize that this internal calibration applied to convert the signal count output

239 to attenuated backscatter units does not always fully represent the actual lidar constant, therefore, it is
240 not accurate enough for meteorological research. Hence, in this study we defined the ceilometer profiles
241 as range corrected signal profiles in arbitrary units.

242

243 Kotthaus et al., (2016) examined the Vaisala CL31 ceilometer by comparing attenuated
244 backscatter profiles from 5 units with different specification of sensor hardware, firmware and operation
245 settings (noise, height and time reporting interval). Research findings show the instrument characteristics
246 that affect the quality and availability of the attenuated backscatter profiles are as follows: At high
247 altitudes, a discontinuity in the attenuated backscatter profile is evident at two height points, ~ 4949 and
248 7000 m. Background signals (instrument related) and cosmetic shift (firmware dependent) tend to be
249 either negative or positive up to 6000m and then switch signs above ~ 6000 m. Below 70 m an overlap
250 correction is applied internally by the ceilometer sensor as well as an obstruction correction (below 50
251 m). Between 50-80 m hardware related perturbation cause a slight offset in the attenuated backscatter
252 values. The authors advise the user-defined reporting interval should be no shorter than 30s to avoid
253 consecutive profiles partial overlap. Background noise reduction can be achieved by a procedure based
254 on long averaging period at nighttime during a clear atmosphere. A range corrected attenuated backscatter
255 can be derived by the attenuated backscatter profiles during an existence of a stratocumulus cloud.

256

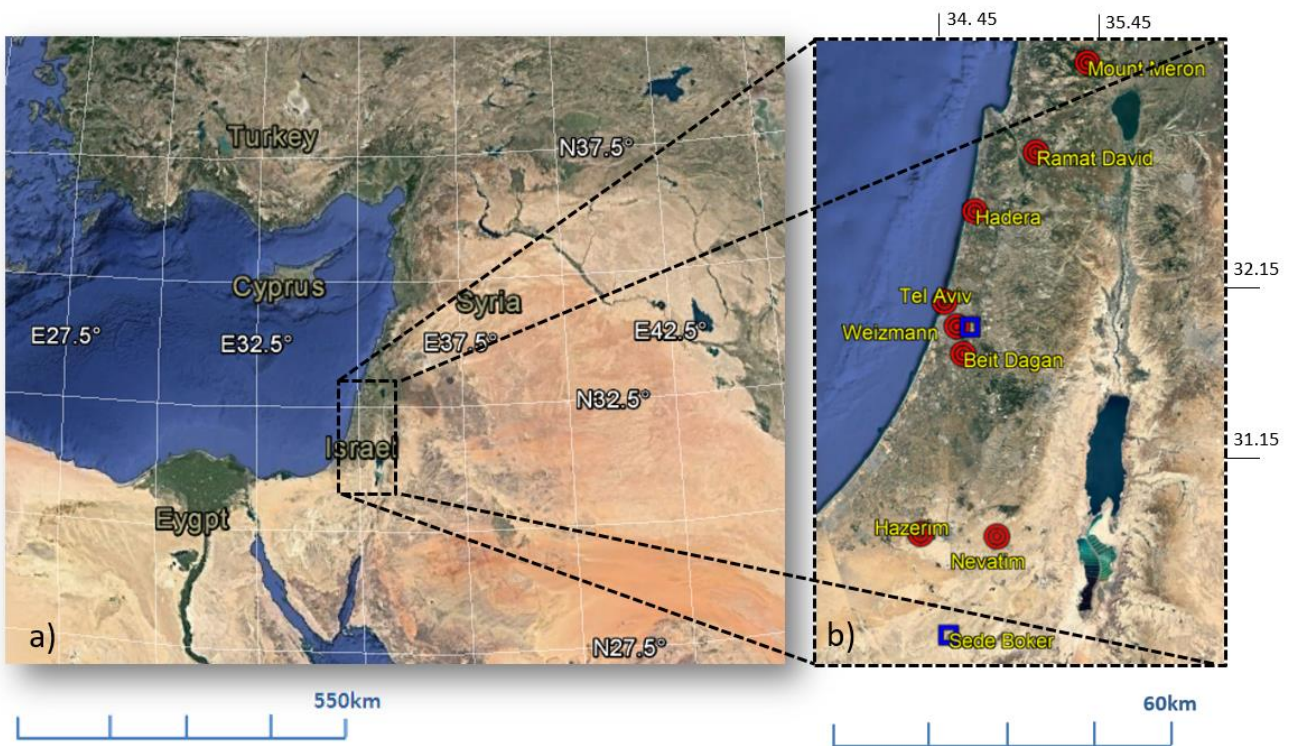
257 Weigner et al, (2014) studied different retrieval methods to derive the aerosol backscatter
258 coefficient from the ceilometers' attenuated backscatter profiles based on a comparison to auxiliary
259 collocated instruments such as a Sunphotometer or a multiwavelength lidar. They focused on calibration
260 methods, the range detection limitations by the overlap function and the sensitivity of the attenuated
261 backscatter signal to relative humidity. Although, the ceilometer wavelength range (given as 905 ± 3 nm)
262 is influenced by water vapor absorption, in the case of aerosol layer detection, water vapor distribution
263 has a small effect on the signal change, indicating the mixed layer height (MLH) or an elevated mixed
264 layer, as the aerosol backscatter itself remains unchanged (Wiegner and Gasteiger, 2015). Consequently,
265 except for a case of a dry layer in a humid MLH, water vapor is unlikely to lead misinterpretation of the
266 aerosol stratification. Fortunately, most algorithms are based on a significant signal slope to define the
267 aerosol layers, therefore, can be determined from uncalibrated ceilometer attenuated backscatter profiles.

268

269 In this research, ceilometer array is comprised of 8 units in different sites (Fig 3 and Tables 2-3),
270 6 of which are owned by a governmental office. The ceilometers are CL31 type apart for ceilometer
271 CL51 stationed in the Weizmann Institute which has a higher backscatter profile range (up to 15.4 km,
272 Munkel et al., 2011). Unfortunately, calibration procedures were not held and maintenance (cleaning of

273 the ceilometer window) was done regularly only in the Beit Dagan ceilometer. Apart from the Beit Dagan
 274 and Weizmann ceilometers we could not retrieve the technical information of firmware and hardware
 275 type (Table 4). However, we have been confirmed (personal communication) that the combination of
 276 hardware and firmware had been done following Kotthaus et al (2016). The Beit Dagan ceilometer signal
 277 count were found to be weaker (up to 800 signal count compared to 10,000 in the other CL31 ceilometers)
 278 due to different hardware definitions. Therefore, in order to present the Beit Dagan range corrected signal
 279 profiles aligned with the profiles of the other ceilometers (given in Fig. 17), the Beit Dagan range
 280 corrected signal values were multiplied by 12.5 (10,000/800). We address the aforementioned limitations
 281 of the ceilometers measurements in the first range gates as we refer to the ceilometer signal count from
 282 100 m AGL. Due to the extreme AOD values of the September dust storm, high extinction of the
 283 ceilometer signal limited the height of profile analyzed down to 1000 m AGL.

284
 285



286
 287 Figure 3. Google Earth map of the large domain (a) and Israel (b) with indications of 8 ceilometer
 288 sites (red circle; detail in Table 2) and two AERONET sites (blue square).

289
 290
 291
 292
 293

2.2 Radiosonde

Radiosonde (RS) type Vaisala RS41-SG is launched by the IMS twice a day at 00 UTC and 12 UTC from the Beit Dagan site adjacent to the Beit Dagan ceilometer. The radiosonde produces profiles of humidity, temperature, pressure, wind speed and wind direction. The output files were downloaded from the University of Wyoming site (<http://weather.uwyo.edu/upperair/sounding.html>, station number 40172). With respect to Stull (1988), the MLH was defined by the RS profiles as the height where an inversion in the temperature was identified along with a significant drop in relative humidity, strong wind shear and an increase in the virtual temperature (Uzan et al., 2016; Levi et al., 2011).

2.3 Particulate matter monitors (PM10, PM2.5)

PM monitors are low-volume flow rate Thermo Fisher Scientific type FH 62 C14 (beta attenuation method) and type 1405 TEOM (Tapered Element Oscillating Microbalance method). Both instruments report PM concentration every 5 min. The location of PM measurement sites is given in Tables 5. In the beta attenuation method (<https://www3.epa.gov/ttnamti1/files/ambient/inorganic/overvw1.pdf>) low-energy beta rays are focused on deposits on a filter tape and attenuated according to the approximate exponential function of particulate mass (i.e., Beer's Law). These automated samples employ a continuous filter tape. The attenuation is measured through an unexposed portion of the filter tape. The tape is then exposed to the ambient sample flow where a deposit is accumulated. The beta attenuation is repeated, and the difference in attenuation between the blank filter and the deposit is a measure of the accumulated concentration. The weighing principle used in the TEOM method (<https://tools.thermofisher.com/content/sfs/manuals/EPM-TEOM1405-Manual.pdf>) is based on a mass change detected by the sensor as a result of the measurement of a change in frequency. The tapered element at the heart of the mass detection system is a hollow tube, clamped on one end and free to oscillate at the other. If additional mass is added, the frequency of the oscillation decreases and a precision electronic counter measures the oscillation frequency with a 10-second sampling period. An electronic control circuit senses oscillation and adds sufficient energy to the system to overcome losses while an automatic gain control circuit maintains the oscillation at a constant amplitude.

327 **2.4 AERONET**

328
329 AEROSOL ROBOTIC NETWORK (AERONET) is multiband photometer with an automatic sun tracking
330 radiometer for direct sun measurements with a spectral range of 340 - 1640 nm wavelengths. The
331 photometer measures the solar extinction in each wavelength to compute aerosol optical depth (Holben
332 et al., 1998). In Israel, AERONET units type CE318-N (<https://aeronet.gsfc.nasa.gov>) operate in Sede
333 Boker and the Weizmann Institute (Fig. 3). Unfortunately, the unit in Weizmann did not operate between
334 6-8 September 2015 due to power failure. For this study, data acquisition was comprised of AOD (500
335 nm wavelength) and Ångström exponent (440-870 nm wavelengths) based on AERONET Level 2.0
336 (cloud screened and quality assured for instrument calibration).

337 338 339 **2.5 Global, direct and diffuse solar radiation measurements**

340
341 Global solar radiation is measured by Kipp & Zonen pyranometer type CMP-11 in 22 sites (Fig. 20)
342 operated by the IMS. The pyranometer produces 10 min measurements of the integrated radiation flux
343 (W m^{-2}) between 300-3000 nm wavelengths. Diffuse and direct radiation are also measured in Beit Dagan
344 (coastal region, 31 m ASL) and Beer Sheva (southern region, 71 m ASL). For diffuse radiation
345 measurements, a ring is mounted over a pyranometer to avoid direct solar radiation. Direct radiation is
346 measured by a sun tracker pyr heliometer.

347 348 349 **2.6 Satellite imagery**

350 351 **2.6.1 SEVIRI (MSG satellite)**

352
353 Meteorological Second Generation (MSG) is a new series of European geostationary satellites operated by
354 EUMETSAT (European Organization for the Exploitation of Meteorological Satellites). On board the
355 MSG is a 12-channel Spinning Enhanced Visible and Infrared Imager (SEVIRI) (Roebeling et al., 2006).
356 The combination of red, blue and green (RGB) channels (red: 10.8-10.4 μm , green: 10.8-8.7 μm , blue: 10.8 μm ,
357 respectively) produce imagery of dust in pink or magenta, dry land in pale blue at daytime and pale green
358 at nighttime. Thick high-level clouds in red-brown tones and thin high-level clouds appear nearly black

359 (<http://oiswww.eumetsat.int/>). Access to EUMETSAT imagery is provided online by
360 <https://www.eumetsat.int/website/home/Images/RealTimeImages/index.html>. Several studies compared
361 AOD from MGS SEVIRI and AERONET measurements (Romano et al., 2013; Bennouna et al., 2009;
362 Jolivet et al., 2008) showed the uncertainty of MSG SEVIRI AOD decreases as AOD rises. For
363 continental aerosol type, errors do not exceed 10 % in viewing zenith angles between 20° and 50. The
364 MSG SEVIRI AOD uncertainty it is expected to be under 15% (Mei et al, 2012) and even higher as the
365 atmospheric AOD increases above 1.5 (EUMETSAT Scientific Validation Report SEVIRI Aerosol
366 Optical Depth (23 Oct 2017). North Africa Sand storm survey (NASCube: <http://nascube.univ-lille1.fr>)
367 obtains AOD by temperature anomalies based on SEVIRI RGB by evaluating the difference in the
368 emissivity of dust and desert surfaces during daytime.

369
370

371 **2.6.2 MODIS (Terra and Aqua satellites)**

372

373 The MODerate resolution Imaging Spectrometer (MODIS) instrument is stationed aboard the Earth
374 Observation System's (EOS) Terra and Aqua polar-orbiting satellites. Terra satellite is on a descending
375 orbit (southward) over the equator at ~ 10:30 local sun time. The Aqua satellite is on an ascending orbit
376 (northward) over the equator at ~ 13:30 local sun time. MODIS performs measurements by 36 channels
377 between 412 -14200 nm whereas the aerosol retrieval makes use of seven channels (646, 855, 466, 553,
378 1243, 1632 and 2119 nm central wavelength) together with a number of other wavelength bands for
379 screening procedures. Remer et al., (2006) revealed errors of 0.01 in the MODIS surface reflectance will
380 lead to errors on the order of 0.1 in AOD retrieval. However, under conditions of high AOD (>1.5) the
381 uncertainty is expected to rise.

382
383

384 **2.6.3 CALIOP (CALIPSO satellite)**

385

386 The Cloud-Aerosol Lidar with Orthogonal Polarization (CALIOP) is a two-wavelength polarization lidar
387 (1064 and 532nm) aboard the Cloud-Aerosol Lidar and Infrared Pathfinder Satellite Observations
388 (CALIPSO) that performs global profiling of aerosols and clouds in the troposphere and lower
389 stratosphere. CALIOP measures signal returns in a large range, from aerosol-free region up to strong
390 cloud returns. The CALIOP profiles are given below 40 km for the 532 nm channel and below 30 km for
391 the 1064 nm channel. Data acquisition in this research was based on level 2 version 4-10 CALIPSO

392 product of 532 nm wavelength with a spatial resolution of 5 km (20N-50N, 20E-50E) and vertical
393 resolution of 60 m (limited up to 6 km).

394

395

396

397 **3. Results and discussion**

398

399 The following description of the dust event will proceed chronologically from 7 to 10 September and
400 include main findings from the different measuring instruments (Sect. 2). The order of the instruments
401 described follow the most interesting features revealed, not necessarily in the same order for each day.
402 We provide 2D ceilometer plots (height vs. time) presenting the extreme dust plume decent only from ~
403 1km ASL due to the ceilometer limitation to detect signals from higher levels (explained in Sect. 2.1).
404 Unlike the high resolution ceilometers, CALIPSO overpass above Israel was available only on 10
405 September 2015 revealing dust distribution in various levels up to 5 km ASL.

406

407

408 **3.1 7 September 2015**

409

410 On 7 September, images from MODIS Aqua (Fig. 4a) and MODIS Terra (Fig. 4e) taken between
411 07:20-12:10 UTC show that the dust plume progressed from northeast in a near-circular motion over the
412 Mediterranean Sea. The penetration of the dust plume to Israel was indicated by AERONET Sede Boker
413 site at ~ 05 UTC by an increase in AOD along a decrease in the Angström exponent (Fig. 5). The
414 connection between decreasing Angström exponent values and the dust plume was pointed out by
415 Mamouri et al., (2016) which presented values of linear depolarization ratio between 0.25-0.32 on 7 and
416 10 September, indicting the dominance of mineral dust. In addition, an increase in the PM concentration
417 started at ~ 05 UTC (not shown) reaching the highest hourly values of $107 \mu\text{g m}^{-3}$ PM_{2.5} (Table 5) and
418 $491 \mu\text{g m}^{-3}$ PM₁₀ (Table 6) only in the Jerusalem elevated sites (~ 800 m ASL) and only at 22 UTC. This
419 17-hour gap is shown by the ceilometers' plots (Fig. 6-12) as a downward motion of the dust plume from
420 ~ 04 UTC in all measuring sites except for the elevated Mount Meron site (1150 m ASL, Fig. 13).
421 Following Gasch et al (2017) cold pool outflows concept, the exception of Mount Meron site is supported
422 by the MSG-SEVIRI picture (Fig. 14) showing that the first dust plume was fragmented (Fig.14, red
423 arrow) and the second dust plume (Fig.14, black arrow) had not passed over Israel before 12 UTC. The
424 deep blue scale evident in all Mount Meron ceilometer plots (Fig. 13) indicate total attenuation

425 distinctively from 7 September ~ 14 UTC to 8 September ~ 16 UTC. However, due to the complexity of
426 the dust plume progress (further shown) and the weak signal counts shown up to 3.5 km ASL (before 7
427 September ~ 14 UTC and after 8 September ~ 16 UTC), the assumption of a total attenuation throughout
428 the period analysed is uncertain. Unfortunately, we did not have auxiliary measurements from the Mount
429 Meron region to justify our assumptions.

430

431 While the MSG-SEVIRI picture at 12 UTC shows AOD values to be under 1 in most parts of
432 Israel (Fig. 15), the PM concentrations on ground level were found to be bearable (up to $105 \mu\text{g m}^{-3}$
433 $\text{PM}_{2.5}$ and $305 \mu\text{g m}^{-3}$ PM_{10} , mainly in the Jerusalem elevated sites). At 12 UTC, Beit Dagan radiosonde
434 profiles show a characteristic MLH of 700 m ASL (Fig. 16). Moreover, at 23 UTC the formation of
435 clouds was indicated by ceilometers' profiles (Fig. 17 a) at 400 m ASL in the shoreline (Tel Aviv, 5 m
436 ASL) and up to ~700 m ASL in the elevated southern site (Nevatim, 400 m ASL). Clouds are identified
437 by the peak shape of the ceilometer profiles (Uzan et al, 2016) and the high range corrected signal of 10
438 $\text{m}^{-1} \text{sr}^{-1}$ which in this case was 4 orders of magnitude higher than the range corrected signal of the dust
439 plume (shown in Fig 17 b-c). Hourly solar radiation measurements (Fig. 18, see 7 September daily plot)
440 from Beit Dagan (central site) and Beer Sheva (southern site) show a significant effect of the dust plume
441 by a decrease in direct radiation along with an increase of diffuse radiation.

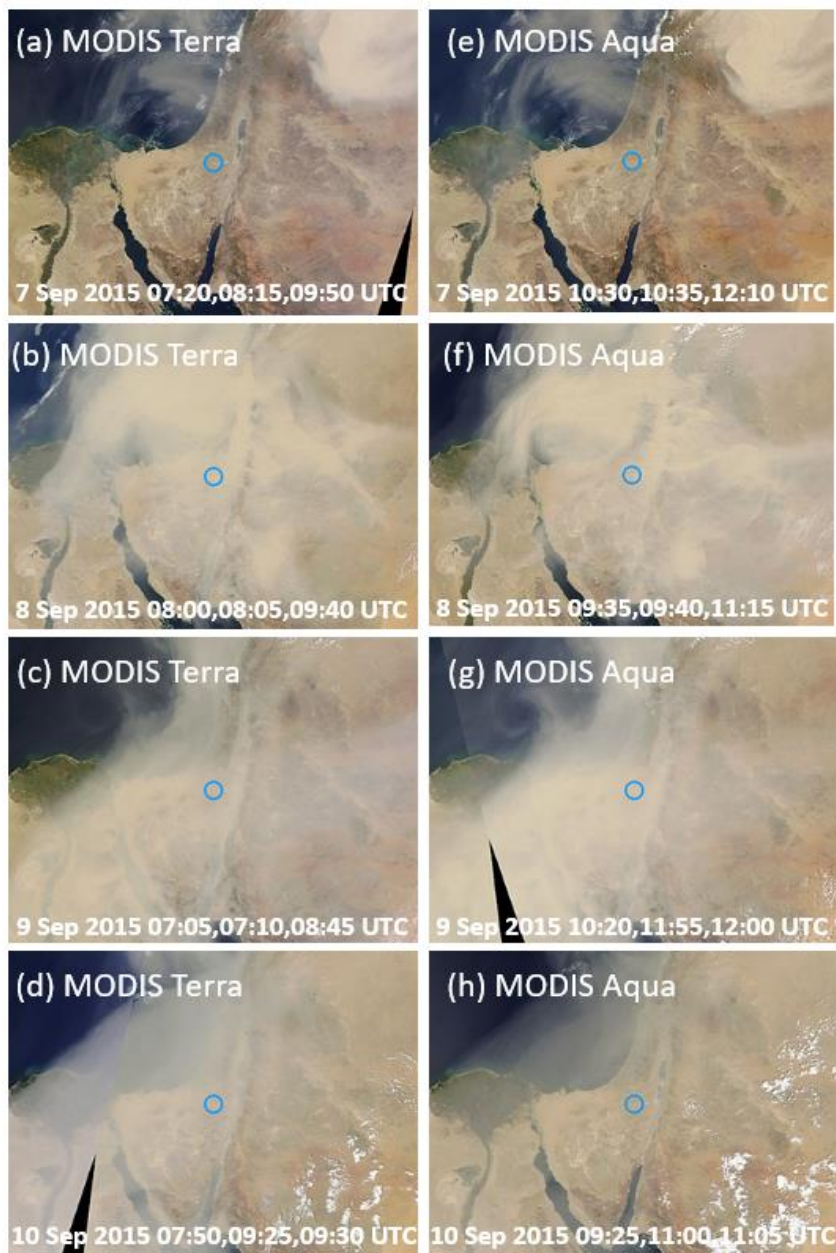
442

443

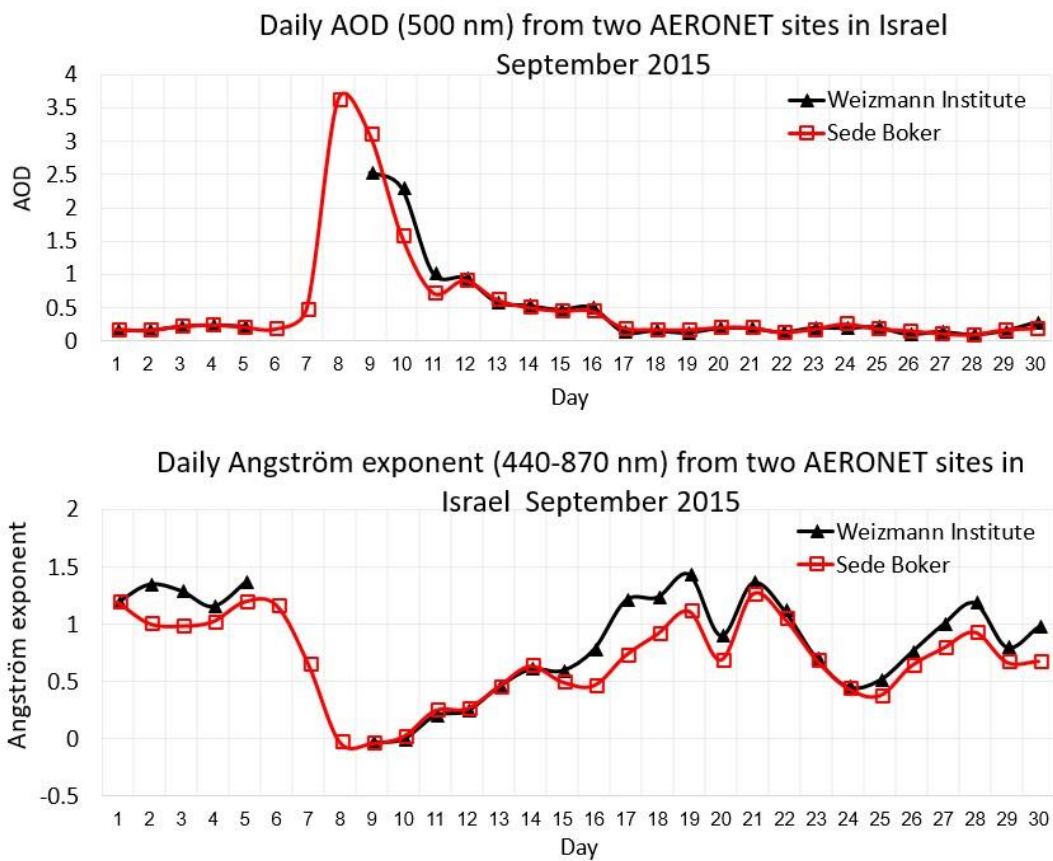
444

445

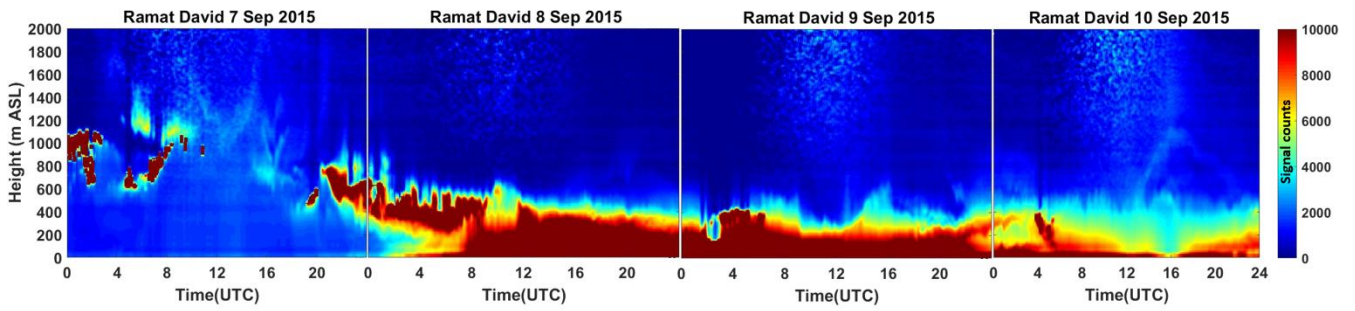
446



447
 448 Figure 4. Pictures from MODIS terra (a-d) and MODIS Aqua (e-h). The date and time of overpass
 449 are indicated on each figure. The blue circle indicates the location of the AERONET Sede Boker
 450 site. Source: <https://aeronet.gsfc.nasa.gov>.
 451
 452
 453
 454
 455
 456
 457
 458



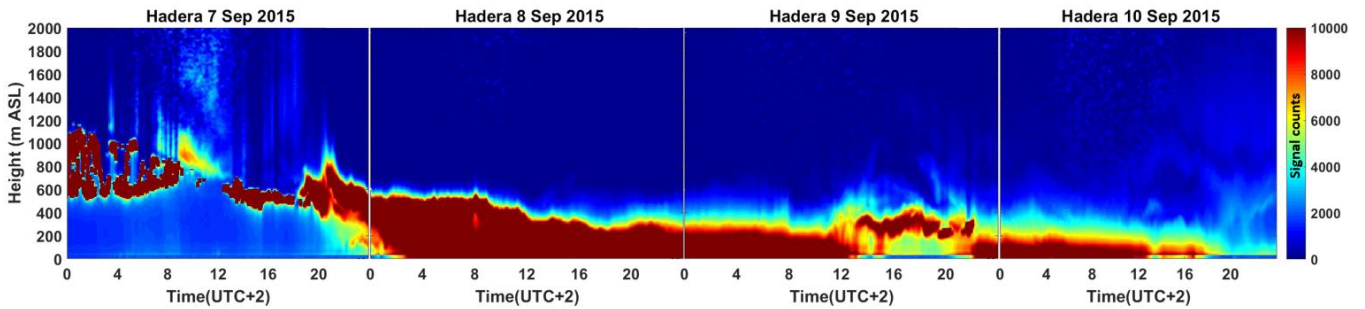
459
 460 Figure 5. September 2015 daily average of AOD (top panel) and Angström exponent (bottom
 461 panel) from two AERONET sites in Israel (Sede Boker and Weizmann, see Fig.3). The
 462 Weizmann AERONET did not operate on 6-8 September due to power failure.
 463
 464
 465
 466
 467
 468
 469
 470
 471
 472
 473
 474



475

476 Figure 6. Ramat David ceilometer signal counts plots for 7-10 September 2015. Y-axis is the height
 477 up to 2000 m ASL, X-axis is the time in UTC, signal count scale range between 0-10,000.

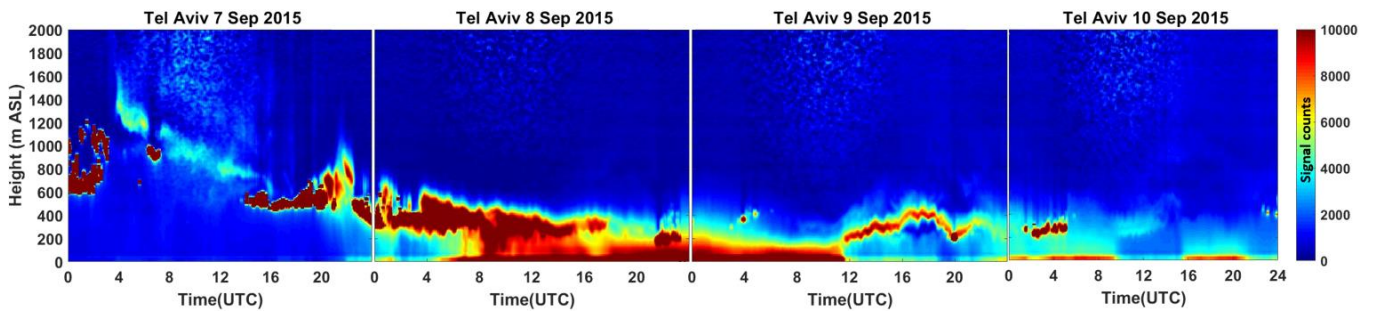
478



479

480 Figure 7. Hadera ceilometer signal counts plots for 7-10 September 2015. Y-axis is the height from
 481 site deployment to 2000 m ASL, X-axis is the time in LST (UTC+2), signal count scale range between
 482 0-10,000.

483

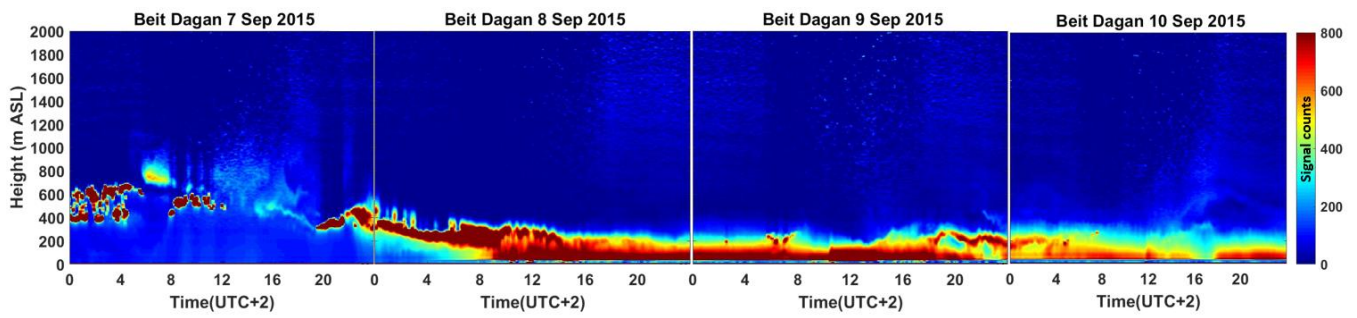


484

485 Figure 8. Tel Aviv ceilometer signal counts plots for 7-10 September 2015. Y-axis is the height from
 486 site deployment to 2000 m ASL, X-axis is the time in UTC, signal count scale range between 0-
 487 10,000.

488

489



490

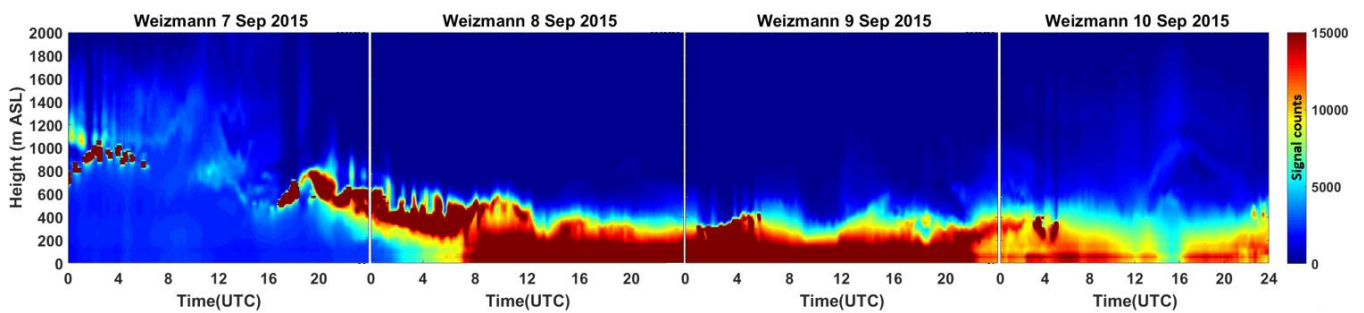
491

492

493

494

Figure 9. Beit Dagan ceilometer signal counts plots for 7-10 September 2015. Y-axis is the height from site deployment to 2000 m ASL, X-axis is in LST (UTC+2), signal count scale range between 0-800.



495

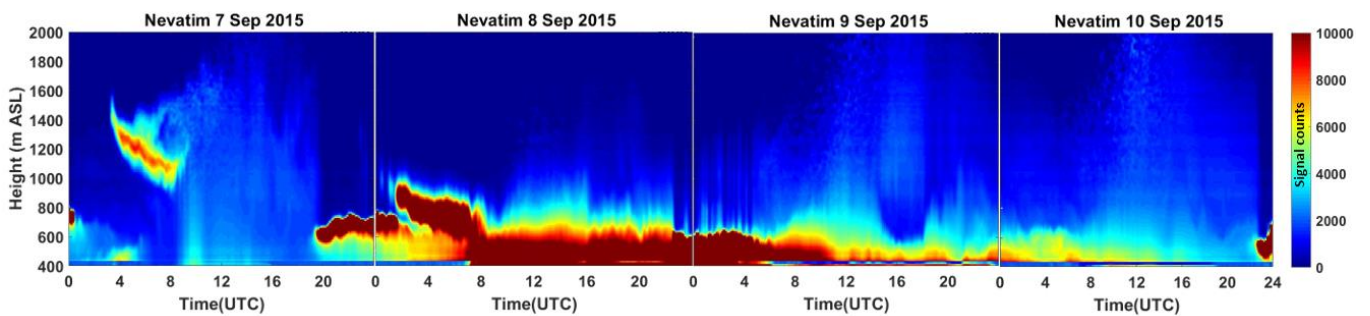
496

497

498

499

Figure 10. Weizmann ceilometer signal counts plots for 7-10 September 2015. Y-axis is the height from site deployment to 2000 m ASL, X-axis is in UTC, signal count scale range between 0-15,000.



500

501

502

503

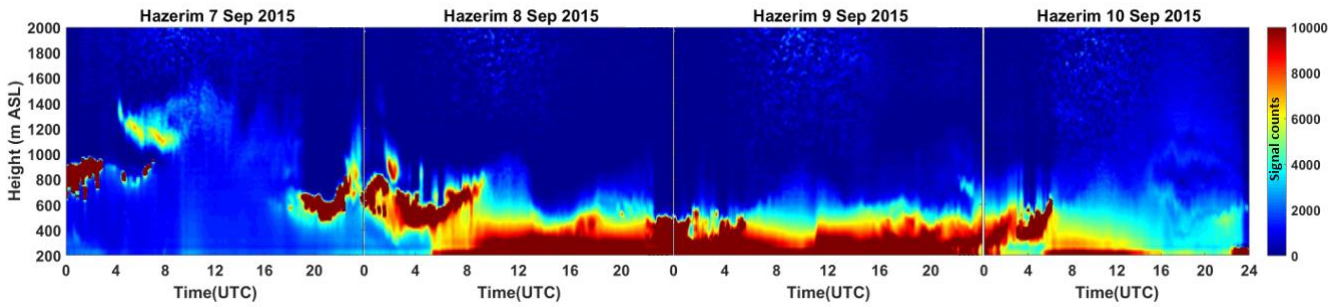
504

505

506

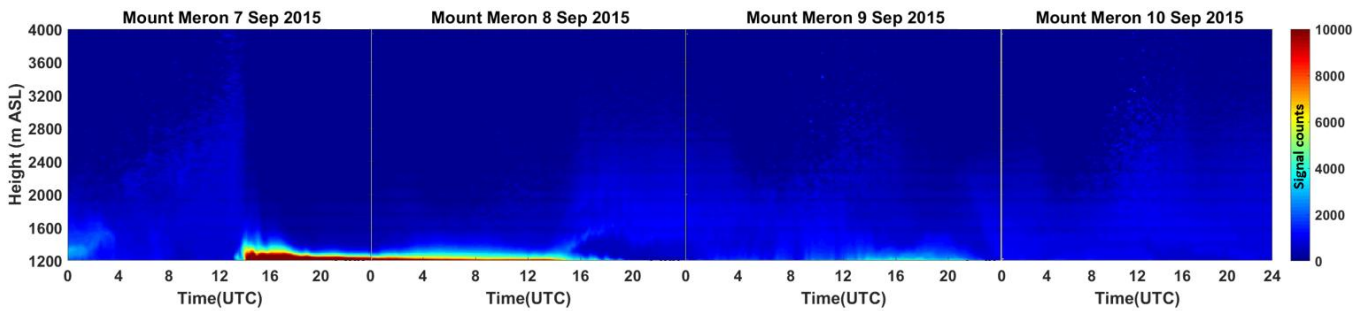
507

Figure 11. Nevatim ceilometer signal counts plots for 7-10 September 2015. Y-axis is the height from site deployment to 2000 m ASL, X-axis is the time in UTC, signal count scale range between 0-10,000.



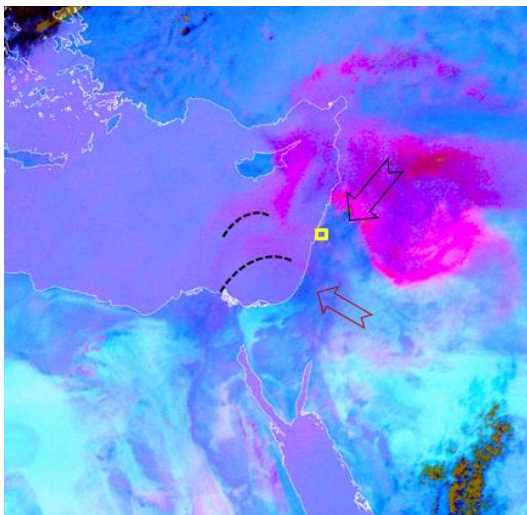
508
509
510
511
512
513

Figure 12. Hazerim ceilometer signal counts plots for 7-10 September 2015. Y-axis is the height from site deployment to 2000 m ASL, X-axis is the time in UTC, signal count scale range between 0-10,000.



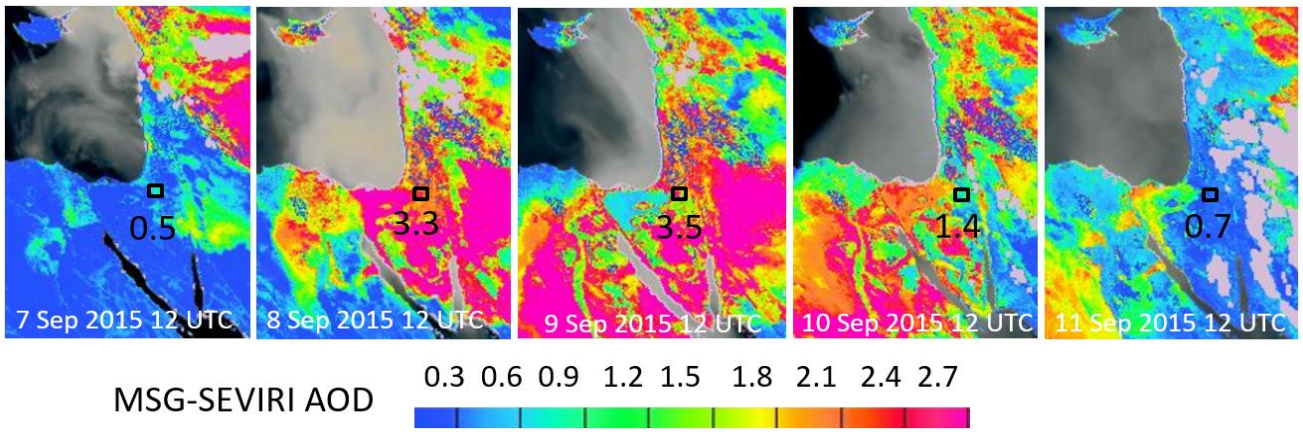
514
515
516
517
518
519
520

Figure 13. Mount Meron ceilometer signal counts plots for 7-10 September 2015. Y-axis is the height from site deployment to 4000 m ASL, X-axis is the time in UTC, signal count scale range between 0-10,000.



521
522
523
524
525

Figure 14. Picture from MSG-SEVIRI satellite of the dust RGB component (dust appears in pink colors) on 7 September 2015 12 UTC with indications of Mount Meron ceilometer site (yellow square, Lon 33.0°, Lat 35.4°) and the dust plumes progression from east to west (red arrow and dashed lines) and from the northeast to southwest (black arrow).



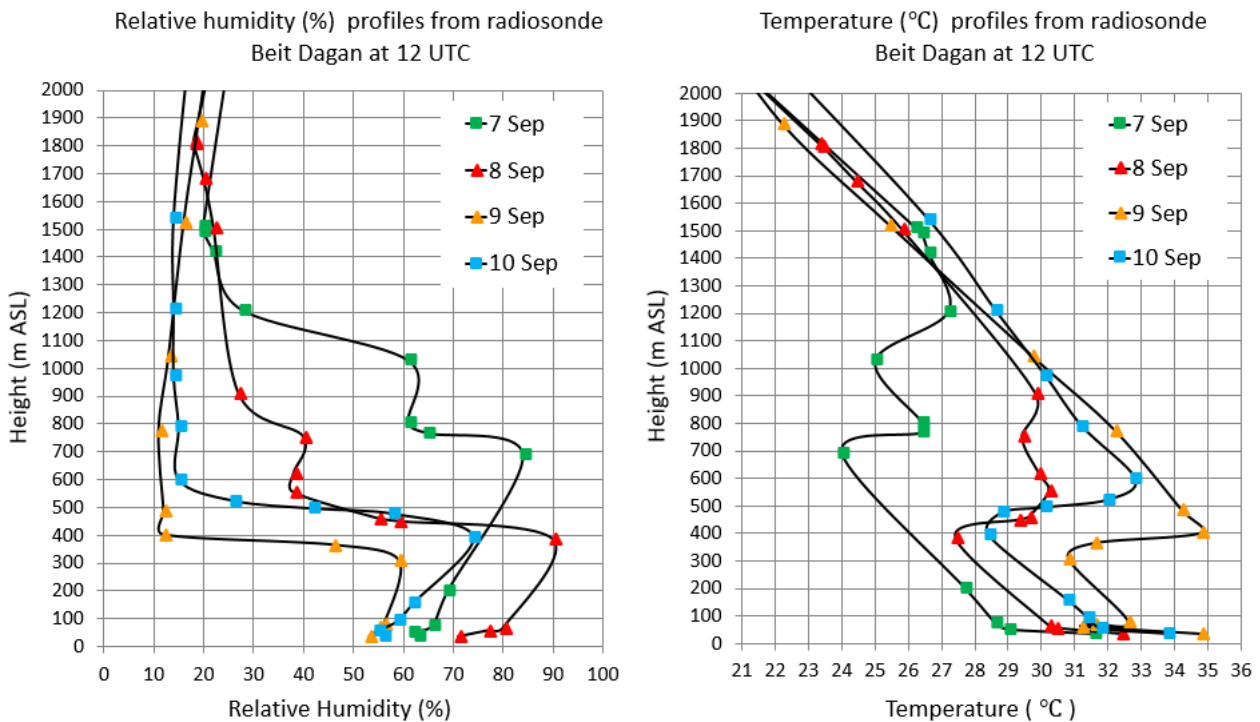
526

527

528 Figure 15. Aerosol Optical Depth (AOD) at 12 UTC 7-11 September 2015 analyzed by NASCube
 529 (Université de Lille) based on imagery from the MSG-SEVIRI satellite (by a combination of the SEVIRI
 530 channels IR8.7, IR10.8 and IR12.0). The map includes indication of the Sede Boker AERONET site
 531 (black square) and its AOD value at 12 UTC.

532

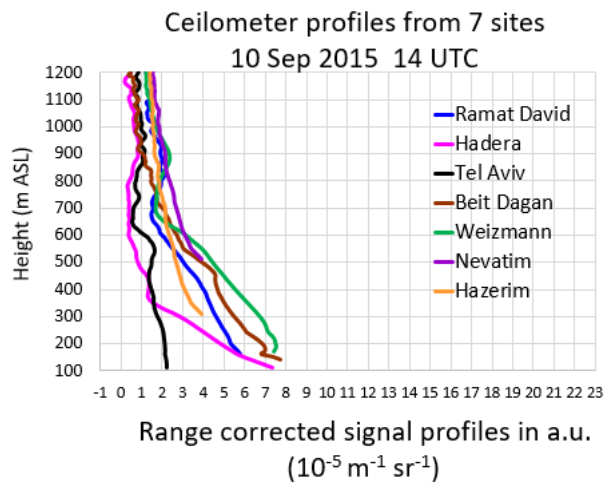
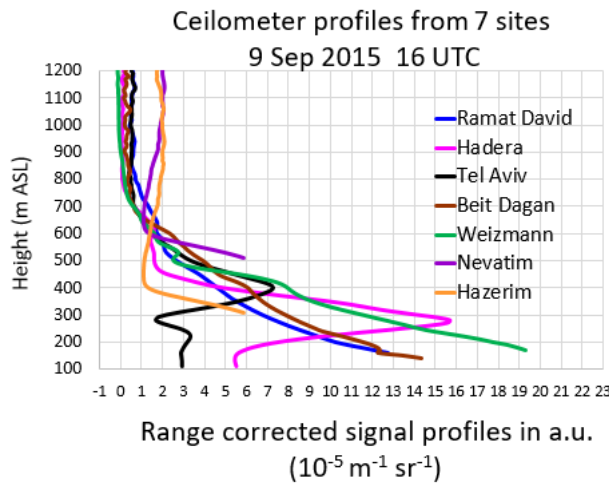
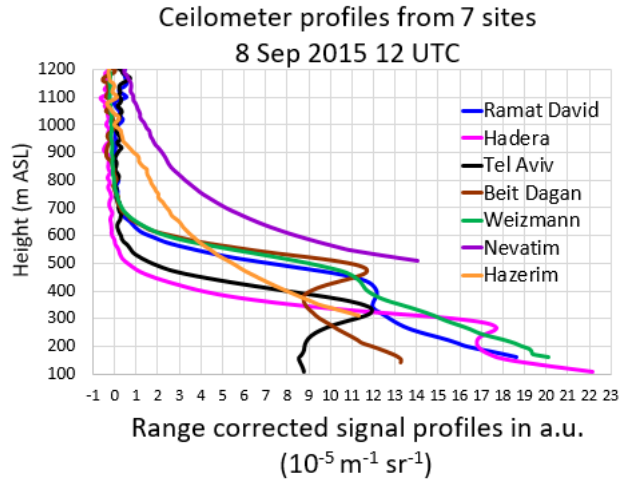
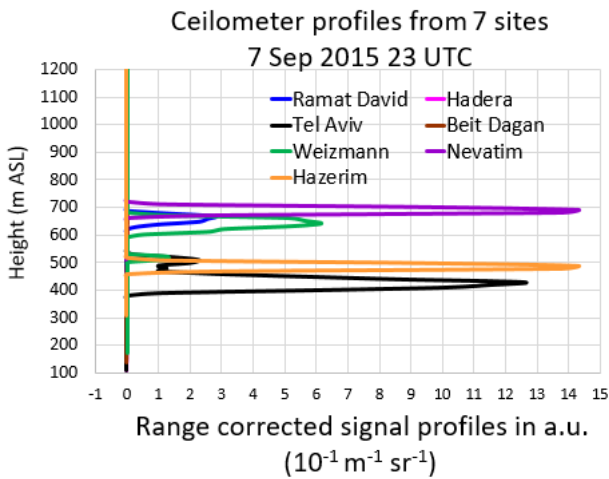
533



534

535 Figure 16. Radiosonde Beit Dagan profiles at 12 UTC between 7-10 September 2015 of relative
 536 humidity (left panel) and temperature (right panel).

537



538
 539 Figure 17. Ceilometer range corrected signal profiles (in arbitrary units) from 7 sites (Ramat
 540 David, Hadera, Tel Aviv, Beit Dagan, Weizmann, Nevatim and Hazerim, see locations in Fig. 3)
 541 on 7 Sep 2015 23 UTC (a), 8 September 2015 12 UTC (b), 9 September 2015 16 UTC (c) and 10
 542 September 2015 14 UTC (d). Notice each profile begins relatively to the height of its' measuring
 543 site (ASL) including a deletion of data from the first 100 m AGL due to inaccuracies in the first
 544 range gates of the ceilometers (for details see Sect. 2.1). Fig (a) shows cloud detection therefore
 545 it is given in a different scale ($10^{-1} \text{ m}^{-1} \text{ sr}^{-1}$) and a different x-axis range.

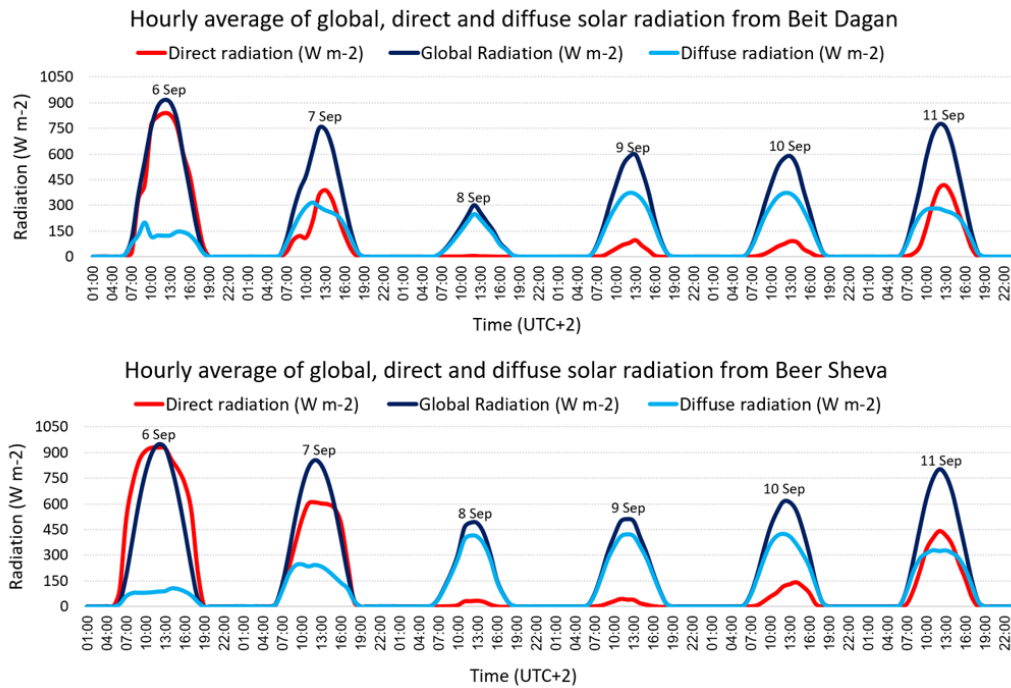


Figure 18. Hourly average of global, direct and diffuse solar radiation between 6-11 September 2015 from Beit Dagan and Beer Sheva.

3.2 8 September 2015

The main phase (the peak) of the dust storm occurred on 8 September. Images from MODIS Aqua (Fig. 4b) and MODIS Terra (Fig. 4f) taken between 08:00-11:15 UTC show the dust storm prevailed over Israel. Ceilometers' plots detect the descending motion of the dust plume reached ground level at ~ 08 UTC (Fig. 6-12). Simultaneously, Sede Boker AERONET AOD measurements increased up to ~4 along with a negative Angström exponent (not shown).

An hour later, at ~ 09 UTC, extreme maximum PM hourly values were measured in the elevated sites of Jerusalem Safra ($10,280 \mu\text{g m}^{-3}$ PM₁₀) and Jerusalem Bar Ilan ($3,063 \mu\text{g m}^{-3}$ PM_{2.5}). Whereby, in the coast and the lower northern regions, maximum PM values were measured only 14 hours later at ~23 UTC and were much lower (up to $3,459 \mu\text{g m}^{-3}$ PM₁₀ and $470 \mu\text{g m}^{-3}$ PM_{2.5}, see Tables 5-6). Fig. 19 illustrates the spatio-temporal variation of the PM₁₀ extreme values, beginning at ~ 12 UTC in the elevated Jerusalem sites and ending at midnight in the shoreline.

At ~08 UTC ceilometer plots from Tel Aviv, Beit Dagan, Weizmann and Hadera (with a higher scale range of 0-15,000, not shown here) reveal an ununiformed dust layer, (beneath and above ~ 300 m

571 ASL) that eventually combined into one dense layer. This process may explain the spatial variation and
572 time delay between the extreme PM measurements in the elevated vs. lower sites.

573

574 MSG-SEVIRI at 12 UTC estimated AOD to be 2.7 while Sede Boker AERONET measured a
575 higher value of 3.3 (Fig. 15). Furthermore, MODIS images (Fig. 4a, 4b) show a dominant dust plume
576 over Israel, whereas solar global radiation measurements (Fig.20a) present significant spatial variations
577 as minimum values (down to 200 W m^{-2}) were measured mainly in northern Israel. Additionally, in spite
578 the extreme PM₁₀ values of $9,031 \mu\text{g m}^{-3}$ measured in the elevated southern site (Negev Mizrahi 577 m
579 ASL, Table 6), the maximum global radiation in southern Israel was still relatively high ($\sim 500 \text{ W m}^{-2}$).
580 Generally, the radiative transfer analysis during heavy dust loads is complicated and relies on several
581 parameters such as size, structure and composition of the aerosols (Bauer et al, 2011). Dense dust layers
582 such as in this extreme dust storm definitely had an impact on the radiation budget hence changing
583 weather patterns and air mass transport. The spatial variation of ground level measurements compared to
584 the quit uniform picture revealed by the satellites may infer the complexity of the dust plume evolution.

585

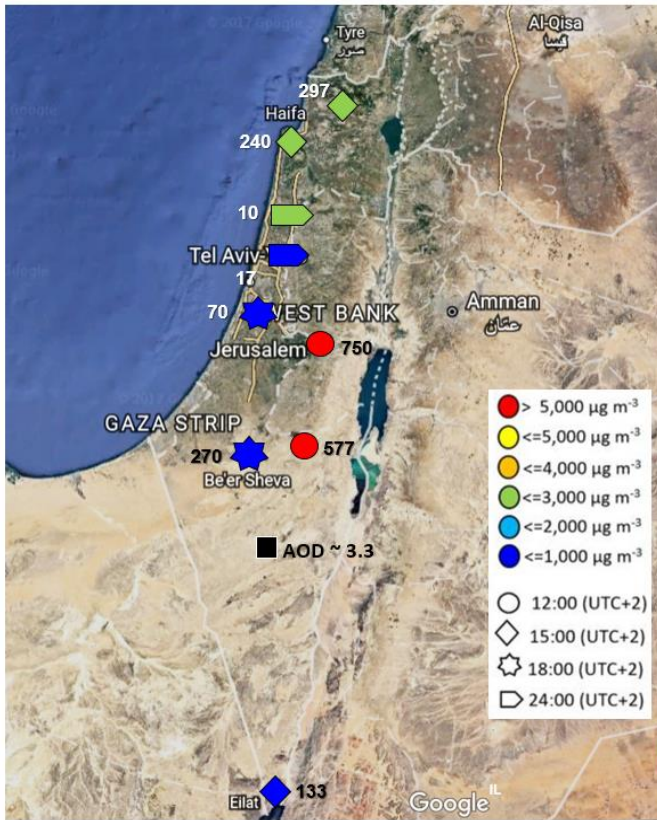
586 Overall, 8 September shows the highest PM concentrations and the lowest solar radiation levels
587 for this dust storm event. The solar radiation was composed mainly of diffuse radiation (Fig.18)
588 emphasizing the immense atmospheric dust loads preventing direct insolation. Surprisingly, the low solar
589 radiation was still capable to warm the ground and generate a late and weak sea breeze front (not shown).
590 We assume the insufficient ground heating generated weak thermals that could not inflate a MLH.
591 Therefore, we assume the low MLH (300 m ASL) revealed by radiosonde Beit Dagan profiles from 8
592 September (Fig.16) may indicate the dust plume base height. As a result, the ceilometers' plots were fully
593 attenuated above $\sim 300 \text{ m ASL}$.

594

595

596

597



598
 599 Figure 19. A map of PM10 maximum hourly concentrations from 9 sites measured on 8
 600 September 2015 10 UTC (midday). The map includes indications of the time of measurement
 601 (symbol shape), concentration range (symbol color), height of measurement site (numbers on
 602 map) and AOD from AERONET Sede Boker site.

598
 599
 600
 601
 602
 603
 604

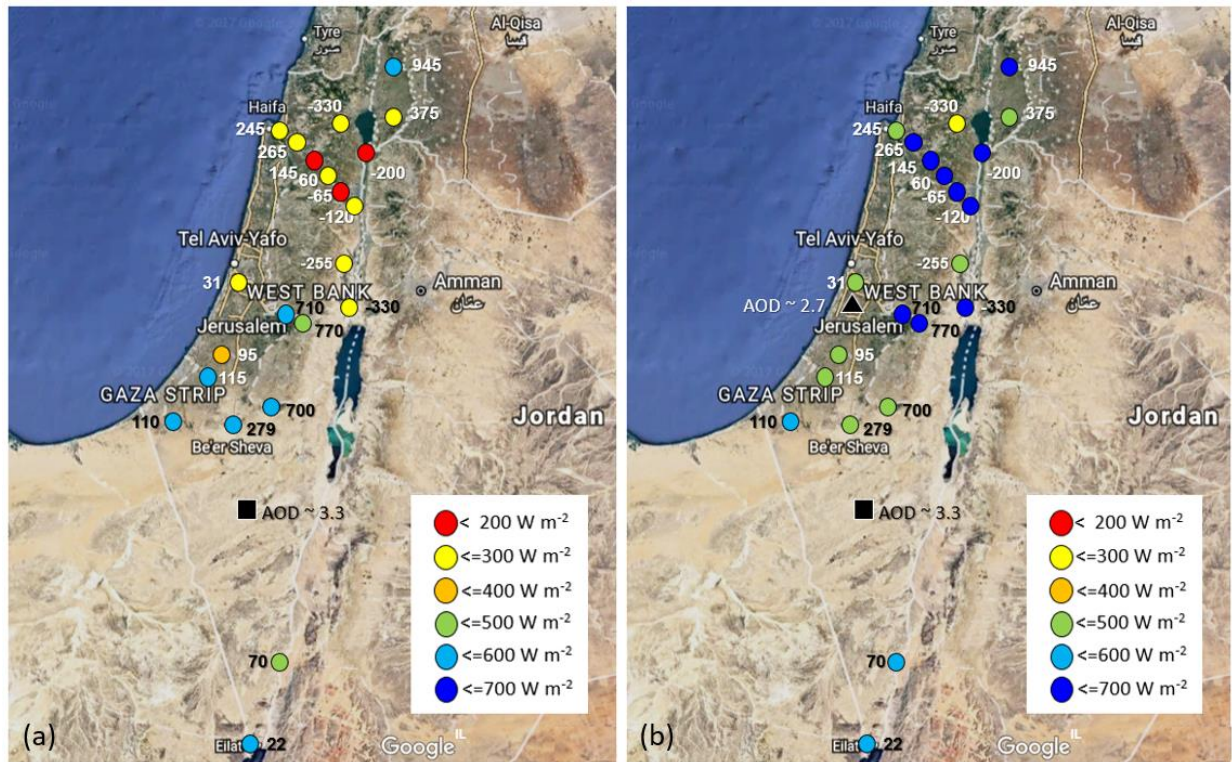


Figure 20. A map of maximum global solar radiation from 22 sites measured at 10 UTC (midday) on 8 September 2015 (a) and on 9 September 2015 (b). The map includes indications of radiation range (see legend), height of measurement site (numbers on the map) and AOD from AERONET Sede Boker site (black square) and Weizmann site (black triangle). On 8 September the AERONET in Weizmann site did not operate due to power failure.

3.3 9 September 2015

On 9 September, MODIS images (Fig.4c and 4g) taken between 07:05-12:00 UTC show the dust plume progression southward to Egypt (Fig. 4), indicated by Sede Boker AERONET AOD >3 along a negative Angström exponent (Fig. 5). At 12 UTC AOD from MSG-SEVIRI is ~ 2.7 whereas Sede Boker AERONET AOD reached up to ~ 3.5 (Fig.15). In contrary to the high AOD measurements, and the descend of the MLH down to ~ 350 m ASL (Fig.16), PM values did not increase but rather decrease below $900 \mu\text{g m}^{-3}$ PM_{2.5} (Table 5) and $4050 \mu\text{g m}^{-3}$ PM₁₀ (Table 6). The drop in PM concentration gave rise to an increase of solar radiation up to 400 W m^{-2} (Fig. 20 b). An increase in solar radiation enables significant ground heating to values measured prior to the initiation of the dust storm (not shown). Thus, allowing generation of thermals and the creation of a late the sea breeze cycle (Uzan et al., 2016). The entrance of the sea breeze front between 11- 12 UTC eventually produced a narrow dust layer ascent visible in mainly in the coastline -Tel Aviv and Hadera ceilometers (Fig.7-8). Interestingly, on 9

626 September, compared to the peak of the dust storm on the day before, we do not see a significant
627 difference in solar radiation in southern Israel, which continued to be relatively high $\sim 500 \text{ W m}^{-2}$ (Fig.
628 20b).

629

630 **3.4 10 September 2015**

631

632 On 10 September, MODIS pictures from 7:50 -11:05 UTC (Fig. 4d and 4h) show the dust plume
633 over Israel transported southeast from Syria-Iraq to Sinai-Egypt. The CALIPSO single overpass Israel at
634 11:00-11:10 UTC revealed a dust layer up to 5 km ASL (Fig.21). This corresponds with the EARLINET
635 lidar measurements in Limassol, Cyprus (Mamouri et al., 2016) detecting a dust plume between 1-3 km
636 ASL. We assume the CALIOP lidar did not produce data beneath 2 km ASL due to total attenuation.
637 Fortunately, the ceilometers complement the dust profile (beneath ~ 1 km ASL) showing a reduction
638 both in signal counts (Fig. 6-12) and in range corrected signal profiles (Fig.17d) pointing out a reduction
639 in atmospheric dust loads. AOD from MSG-SEVIRI and Sede Boker AEONET show a decrease down
640 to ~ 1.5 and a low Angström exponent of ~ 0.5 indicating prevalence of mineral dust.

641

642 A profound reduction in PM values, down to a third of the values from the day before (Table 6),
643 was evident mainly in southern Israel. Therefore, an increase in direct radiation was measured in southern
644 site (Fig.18). The reduction of dust loads may also be denoted by the orange background color of the
645 photograph taken on 8 September (Fig.1b) compared to the grey background visible on 10 September
646 (Fig.1c). As the dust storm dissipated, cloud formation (indicated by brown spots and evaluated by
647 ceilometer profiles -not shown) was visible from ~ 4 UTC by ceilometers Ramat David (Fig.6), Tel Aviv
648 (Fig.8), Weizmann (Fig.10) and Hazerim (Fig.11). the clouds formation was not evident by MODIS
649 imagery (Fig 4d, 4h).

650

651

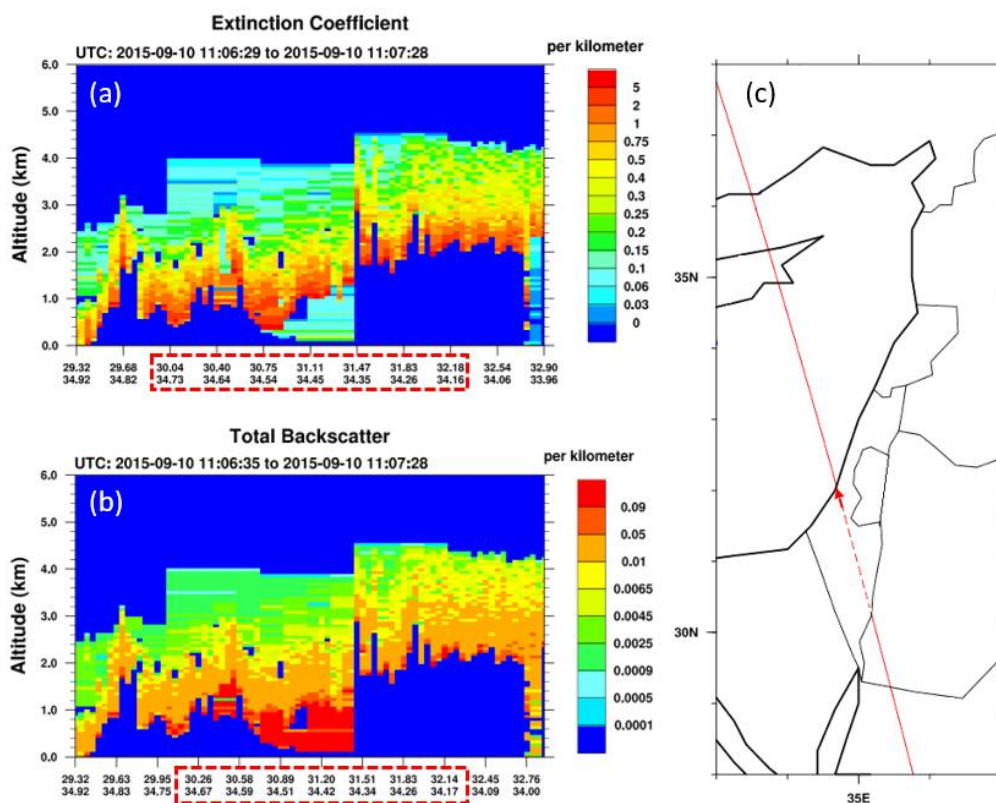


Figure 21. (c) A map of the EM centered on Israel with indication of CALIPSO satellite overpass from south-east to north-west (red line) on 10 September 2015 11:00-11:10 UTC. CALIOP lidar products (from 532 nm wavelength) of extinction coefficient (a) and total backscatter (b) are given along the path over Israel (dashed red line). The ground elevation begins from -20 m ASL in the southeastern point. A quarter of the way through ground level rises up to ~ 600 m ASL and then gradually declines to sea level height as it reached shoreline in the northwestern point.

In the attempt to determine the "end" of the dust storm over Israel, we analyzed measurements from all instruments (Sect. 2) seeking values that were measured prior to the dust storm penetration. AERONET AOD values (Fig.5), solar radiation measurements (not shown) and satellite imagery from MODIS and SEVIRI (not shown) indicate clearance of the dust storm on 17 September. On the other hand, PM values and ceilometer profiles indicated the dust storm ended 4 days earlier on 13 September (not shown). The difference between the measurements that include atmospheric layers aloft (satellite imagery, solar radiation and AOD AERONET) compared to measurements limited to the lower atmosphere (PM values and ceilometers) postulates a scheme of several dust layers or multiple sources of the dust plumes, which may support similar conclusions from previous studies (Stavros et al, 2016; Mamouri et al, 2016, Gasch et al, 2017).

4. Conclusions

A very severe dust storm struck the EM on September 2015. Previous investigations presented in-situ and remote sensing measurements, discussed the initiation of the dust storm in the Syrian-Iraqi border, aspects of its transport over the EM and the limitations of the models to forecast this unique event. The analysis concentrated mainly on the upper level of the atmosphere at specific time segments of the dust storm. The benefit of this study is the provision of continuous measurements of vertical dust profiles in the lower part of the troposphere from 8 ceilometer sites. The data presented here can be used as a tool to verify state of the art model simulations and provide a different point of view to the meteorological conditions governing the dust plume advection over the EM.

This study confirmed that the dust storm entered Israel on 7 September and showed the gradual downfall of the dust plume from ~1000m ASL on 7 September down to ~400 m ASL on 8 September. The detailed ceilometer profiles and auxiliary instruments enabled to separate the dust storm into separated dust layers (beneath and above 1 km). As the dust plume descended towards ground level on 8 September, PM concentration increased in the elevated stations (up to 10,280 $\mu\text{g m}^{-3}$ PM10) and radiation decreased down to ~200 W m^{-2} mainly in the northern region.

On 9 September, in spite of the high AOD (above 3), the global radiation (mainly comprised of diffuse radiation) increased, thus enabling sufficient ground heating for the creation of a late sea breeze front (between 11-12 UTC). The sea breeze circulation generated a narrow dust layer detached from the ground in the coastal region (Tel Aviv, Hadera and Beit Dagan).

On 10 September, the dust plume motion continued southwest to Egypt, indicated by CALIPSO as dust layers up to 5 km. The end of the dust storm over Israel was indicated on 17 September by satellite imagery, solar radiation and AOD AERONET, while measurements limited to the lower atmosphere (PM values and ceilometers) indicated the dust storm ended on 13 September. The difference between the various instruments suggests a scheme of several dust layers or multiple sources of the dust plumes.

To conclude, Ceilometers have been found to be a crucial tool in the study of the September dust storm evolution over Israel. In general, ceilometers provide high resolution data base (temporal and spatial) that broaden the scope of the atmospheric measurements. Fortunately, as worldwide ceilometer deployment expands, ceilometers are realized as an essential tool in the analysis of meteorological phenomena and aerosol transport most valuable in the meso-scale.

5. Data availability

PM10 measurements- Israeli Environmental ministry air quality monthly reports:

<http://www.svivaaqm.net>.

Israeli Environmental ministry air quality monthly reports (in Hebrew):

<http://www.sviva.gov.il/subjectsEnv/SvivaAir/AirQualityData/NationalAirMonitoing/Pages/AirMoritoringReports.aspx>.

Weather reports- Israeli Meteorological Service September monthly report (in Hebrew):

<http://www.ims.gov.il/IMS/CLIMATE/ClimateSummary/2015/hazesept+2015.htm>

Radiosonde profiles –University of Wyoming: <http://weather.uwyo.edu/upperair/sounding.html>.

AERONET data- <https://aeronet.gsfc.nasa.gov>.

Meteosat Second Generation Spacecraft pictures:

http://nascube.univ-lille1.fr/cgi-bin/NAS3_v2.cgi.

<https://www.eumetsat.int/website/home/Images/RealTimeImages/index.html>

Ceilometer profiles- the data is owned by governmental offices. The data is not online and provided by request.

Author contribution

Leenes Uzan carried out the research and prepared the manuscript under the careful guidance of Smadar Egert and Pinhas Alpert. The authors declare that they have no conflict of interest.

Acknowledgements

For the provision of ceilometer data, we wish to thank the Israeli Meteorological Service (IMS), the Israeli Air Force (IDF), Association of towns for environmental protection (Sharon-Carmel) and Rafat Qubaj from the department of Earth and Planetary Science in the Weizmann institute of Science. Special thanks to Nir Stav (IMS) and Dr. Yoav Levy (IMS) for their fruitful advice, Anat Baharad (IMS) for computer assistance and Pavel Kunin (Tel Aviv university) for the CALIPSO images. We thank the principal investigators Prof. Arnon Karnieli and Prof. Yinon Rudich for their effort in establishing and maintaining Sede Boker and Weizmann AERONET sites. We wish to thank the institutes that provide open site data reduction: Université de Lille NASCube, Wyoming University Radiosonde and the Israeli ministry of Environmental protection for the PM data. Partial funding of this research was made by the Virtual Institute DESERVE (Dead Sea Research Venue).

References

- Alpert P., Osetinsky I., Ziv B. and Shafir H.: A new seasons definition based on the classified daily synoptic systems: An example for the Eastern Mediterranean, *Int. J. Climatol.* 24,1013-1021, 2004.
- Alpert, P., Ziv, B.: The Sharav cyclone-observations and some theoretical considerations, *Int. J. Geoph. Res.*, 94, 18495-18514, 1998.
- Ansmann, A., Petzold, A., Kandler, K., Tegen, I.N.A., Wendisch, M., Mueller, D., Weinzierl, B., Mueller, T. and Heintzenberg, J.: Saharan Mineral Dust Experiments SAMUM-1 and SAMUM-2: what have we learned? *Tellus B*, 63(4), 403-429, 2011.
- Bauer, S., Bierwirth, E., Esselborn, M., Petzold, A., Macke, A., Trautmann, T. and Wendisch, M.: Airborne spectral radiation measurements to derive solar radiative forcing of Saharan dust mixed with biomass burning smoke particles. *Tellus B*, 63(4), 742-750, 2011.
- Bennouna, Y.S., De Leeuw, G., Piazzola, J. and Kusmierczyk-Michulec, J.: Aerosol remote sensing over the ocean using MSG-SEVIRI visible images. *Journal of Geophysical Research: Atmospheres*, 114(D23), 2009.
- Continuous measurement of PM10 suspended particulate matter (SPM) in ambient air, Center for Environmental Research Information Office of Research and Development U.S. Environmental Protection Agency Cincinnati, OH 45268 June 1999.
- Dayan U., Lifshitz-Golden B., and Pick K.: Spatial and structural variation of the atmospheric boundary layer during summer in Israel-profiler and rawinsonde measurements, *J. Appl. Meteo.* 41, 447-457, 2002.
- Derimian, Y., Karnieli, A., Kaufman, Y.J., Andreae, M.O., Andreae, T.W., Dubovik, O., Maenhaut, W., Koren, I. and Holben, B.N.: Dust and pollution aerosols over the Negev desert, Israel: Properties, transport, and radiative effect, *J. Geophys. Res.*, 111, D05205 (1-14), 2006.
- Donner, L.J., Wyman, B.L., Hemler, R.S., Horowitz, L.W., Ming, Y., Zhao, M., Golaz, J.C., Ginoux, P., Lin, S.J., Schwarzkopf, M.D. and Austin, J.: The dynamical core, physical parameterizations, and

785 basic simulation characteristics of the atmospheric component AM3 of the GFDL global coupled
786 model CM3, *Journal of Climate*, 24(13), 3484-3519, 2011.

787
788 Dubovik, O., A. Smirnov, B. N. Holben, M. D. King, Y. J. Kaufman, T. F. Eck, and Slutsker I.:
789 Accuracy assessments of aerosol optical properties retrieved from Aerosol Robotic Network
790 (AERONET) Sun and sky radiance measurements, *J. Geophys. Res.*, 105(D8), 9791–9806, 2000.

791
792 Gasch, P., Rieger, D., Walter, C., Khain, P., Levi, Y., Knippertz, P., and Vogel, B.: Revealing the
793 meteorological drivers of the September 2015 severe dust event in the Eastern Mediterranean,
794 *Atmos. Chem. Phys.*, 17, 13573-13604, 2017.

795
796 Haeffelin M., Angelini F., et al: Evaluation of Mixing –Height Retrievals from Automatic Profiling
797 Lidars and Ceilometers in View of Future Integrated Networks in Europe. *Boundary-layer Meteorol.*,
798 143,49-75, 2012.

799
800 Holben, B.N., Eck, T.F., Slutsker, I., Tanre, D., Buis, J.P., Setzer, A., Vermote, E., Reagan, J.A.,
801 Kaufman, Y.J., Nakajima, T. and Lavenue, F.: AERONET—A federated instrument network and data
802 archive for aerosol characterization. *Remote sensing of environment*, 66(1), 1-16, 1998.

803
804 Hsu, N.C., Jeong, M.J., Bettenhausen, C., Sayer, A.M., Hansell, R., Seftor, C.S., Huang, J. and Tsay,
805 S.C.: Enhanced Deep Blue aerosol retrieval algorithm: The second generation. *Journal of*
806 *Geophysical Research: Atmospheres*, 118(16), 9296-9315, 2013.

825
826 Jasim, F.H., Investigation of the 6-9 September 2015 Dust Storm over Middle East, *AJER*, 5 (11),
827 201-207, 2016.

828
829 Jolivet, D., Ramon, D., Bernard, E., Deschamps, P.Y., Riedi, J., Nicolas, J.M. and Hagolle, O.:
830 Aerosol monitoring over land using MSG/SEVIRI. In *Proceeding of the EUMETSAT*
831 *Meteorological Satellite Conference*, Darmstadt, Germany ,8-12, 2008.

832
833 Kaskaoutis, D.G., Kambezidis, H.D., Nastos, P.T. and Kosmopoulos, P.G.: Study on an intense dust
834 storm over Greece. *Atmospheric Environment*, 42(29), 6884-6896, 2008.

836 Koschmieder H.: Theorie der horizontalen sichtweite, Beitrage zur Physik der Freien Atmosphere
837 12, 33–55,171–181, 1924.

838
839
840 Kotthaus, S., O'Connor, E., Munkel, C., Charlton-Perez, C., Gabey, A. M., and Grimmond, C. S. B.:
841 Recommendations for processing atmospheric attenuated backscatter profiles from Vaisala CL31
842 Ceilometers. *Atmos. Meas. Tech.*, 9, 3769-3791, 2016.

843
844 Levi Y., Shilo E., Setter I.: Climatology of a summer coastal boundary layer with 1290-MHz wind
845 profiler radar and a WRF simulation. *J. Appl. Meteo.*, 50(9), 1815-1826, 2011.

846
847 Mamouri, R.E., Ansmann, A., Nisantzi, A., Solomos, S., Kallos, G. and Hadjimitsis, D.G.: Extreme
848 dust storm over the eastern Mediterranean in September 2015: satellite, lidar, and surface
849 observations in the Cyprus region, *Atmos. Chem. Phys.*, 16(21), 13711-13724, 2016.

850
851 Mei, L., Xue, Y., de Leeuw, G., Holzer-Popp, T., Guang, J., Li, Y., Yang, L., Xu, H., Xu, X., Li, C.
852 and Wang, Y.: Retrieval of aerosol optical depth over land based on a time series technique using
853 MSG/SEVIRI data. *Atmospheric Chemistry and Physics*, 12(19), 9167–9185, 2012.

854
855 Mona, L., Liu, Z., Müller, D., Omar, A., Papayannis, A., Pappalardo, G., Sugimoto, N. and Vaughan,
856 M.: Lidar measurements for desert dust characterization: an overview. *Advances in*
857 *Meteorology*, 2012.

858
859 Munkel C., Emeis S., Muller J. W., Schäfer K.: Aerosol concentration measurements with a lidar
860 ceilometer: results of a one year measuring campaign, *Remote sensing of Clouds and the*
861 *Atmosphere VIII*, 5235, 486-496, 2004.

862
863 Munkel, C., Schäfer, K. and Emeis, S.: Adding confidence levels and error bars to mixing layer
864 heights detected by ceilometer, In *Proc. SPIE*, Vol. 8177, 817708-1, 2011.

865
866 Papayannis, A., Amiridis, V., Mona, L., Tsaknakis, G., Balis, D., Bösenberg, J., Chaikovski, A., De
867 Tomasi, F., Grigorov, I., Mattis, I. and Mitev, V.: Systematic lidar observations of Saharan dust over
868 Europe in the frame of EARLINET (2000–2002). *Journal of Geophysical Research:*
869 *Atmospheres*, 113(D10), 2008.

- 870
871 Parolari, A.J., Li, D., Bou-Zeid, E., Katul, G.G. and Assouline, S.: Climate, not conflict, explains
872 extreme Middle East dust storm, *Environ. Res. Lett.*, 11, 114013, 2016.
- 873
874 Pu, B. and Ginoux, P.: The impact of the Pacific Decadal Oscillation on springtime dust activity in
875 Syria, *Atmos. Chem. Phys.*, 16(21), 13431-13448, 2016.
- 876
877 Rao, P.G., Hatwar, H.R., Al-Sulaiti, M.H. and Al-Mulla, A.H.: Summer shamals over the Arabian
878 Gulf. *Weather*, 58(12), 471-478, 2003.
- 879
880 Remer, L.A., Tanre, D., Kaufman, Y.J., Levy, R. and Mattoo, S.: Algorithm for remote sensing of
881 tropospheric aerosol from MODIS: Collection 005. National Aeronautics and Space
882 Administration, 1490, 2006.
- 883
884 Rieger, D., Bangert, M., Bischoff-Gauss, I., Förstner, J., Lundgren, K., Reinert, D., Schröter, J.,
885 Vogel, H., Zängl, G., Ruhnke, R. and Vogel, B.: ICON-ART 1.0-a new online-coupled model system
886 from the global to regional scale. *Geosci. Model Dev.*, 8, 1659–1676, 2015
- 887
888 Roebeling, R. A., Feijt A. J., and Stammes P.: Cloud property retrievals for climate monitoring:
889 Implications of differences between Spinning Enhanced Visible and Infrared Imager (SEVIRI) on
890 METEOSAT-8 and Advanced Very High Resolution Radiometer (AVHRR) on NOAA-17, *J.*
891 *Geophys. Res.*, 111(D20), 2006.
- 892
893 Romano, F., Ricciardelli, E., Cimini, D., Di Paola, F. and Viggiano, M.: Dust Detection and Optical
894 Depth Retrieval Using MSG-SEVIRI Data. *Atmosphere*, 4(1), 35-47,2013.
- 895
896 Scientific Validation Report SEVIRI Aerosol Optical Depth, EUMETSAT Satellite Application
897 Facility on Climate Monitoring, 23 October 2017, doi: 10.5676/EUM_SAF_CM/MSG_AOD/V001.
- 898
899 Solomos, S., Ansmann, A., Mamouri, R.-E., Biniotoglou, I., Patlakas, P., Marinou, E., and Amiridis,
900 V.: Remote sensing and modeling analysis of the extreme dust storm hitting Middle East and Eastern
901 Mediterranean in September 2015, *Atmos. Chem. Phys.*, 17, 4063-4079, 2017.
- 902
903 Stull R. B.: An introduction to boundary layer meteorology, Kluwer Academic publishers,
904 Netherlands, 666p, 1988.

905
906 Uzan L., Alpert P.: The coastal boundary layer and air pollution- A high temporal resolution analysis
907 in the East Mediterranean Coast, The open atmospheric science journal, 6 ,9-18, 2012.

908
909 Uzan, L., Egert, S. and Alpert, P.: Ceilometer evaluation of the eastern Mediterranean summer
910 boundary layer height–first study of two Israeli sites. Atmos. Meas. Tech., 9(9), 4387-4398, 2016.

911
912 Vaisala ceilometer CL31 user's guide M210482EN-B, October, 2004.

913
914 Wang, Y. Q.: MeteoInfo: GIS software for meteorological data visualization and analysis. Met.
915 Apps, 21, 360–368, 2014.

916
917 Wiegner M. and Gasteiger J.: Correction of water vapor absorption for aerosol remote sensing with
918 ceilometers, Atmos. Meas. Tech., 8, 3971–3984, 2015.

919
920 Wiegner, M., Madonna, F., Biniotoglou, I., Forkel, R., Gasteiger, J., Geiß, A., Pappalardo, G., Schäfer,
921 K. and Thomas, W.: What is the benefit of ceilometers for aerosol remote sensing? An answer from
922 EARLINET, Atmos. Meas. Tech., 7(7), 1979–1997, 2014.

923
924 Winker, D.M., Vaughan, M.A., Omar, A., Hu, Y., Powell, K.A., Liu, Z., Hunt, W.H. and Young,
925 S.A.: Overview of the CALIPSO mission and CALIOP data processing algorithms. Journal of
926 Atmospheric and Oceanic Technology, 26(11), 2310-2323, 2009.

939

940

941

942 Table 1. The publications on the September 2015 dust event

Publications	Title	Main Tool	Main outcome
Pu, B. and Ginoux, P (2016)	The impact of the Pacific Decadal Oscillation on springtime dust activity in Syria	MODIS Terra MODIS Aqua DOD AOD, GFDL-AM3 model	Model underestimation in the EM due to inaccurate soil moisture
Parolari et al. (2016)	Climate, not conflict, explains extreme Middle East dust storm	WRF model	Unusual low level westerly wind spread to the EM, to reversely transport the previously eastward particles back to the EM.
Mamouri et al. (2016)	Extreme dust storm over the eastern Mediterranean in September 2015: satellite, lidar, and surface observations in the Cyprus region	MODIS, EARLINET profiles and PM10	Dust plumes from Syria entered the EM in a double layer structure, pointing to multiple dust sources
Solomos et al. (2016)	Remote sensing and modeling analysis of the extreme dust storm hitting Middle East and Eastern Mediterranean in September 2015	RAMS model EARLINET lidar, MSG and CALIPSO.	Low model ability to simulate the event, due to inaccuracies in model physical processes.
Jasim, F.H. (2016)	Investigation of the 6-9 September 2015 Dust Storm over Middle East	Satellite MSG-SEVIRI, Meteoinfo model	Two dust storms simultaneously, from northern Syria and Sinai desert created by two low pressure systems
Gasch et al. (2017)	An analysis of the September 2015 severe dust event in the Eastern Mediterranean	ICON-ART model	An unusual early active Red Sea Trough with meso-scale convective systems generating cold-pool outflows producing the dust storm. Model lacked development of a super critical flow to produce excessive wind speeds

943

944

945

946
947
948
949

Table 2. Ceilometers locations

Location	Site	Long/Lat	Distance from shoreline (km)	Height (m AGL)
Mount Meron	Northern	33.0/35.4	31	1,150
Ramat David	Northern	32.7/35.2	24	50
Hadera	Onshore	32.5/34.9	3.5	10
Tel Aviv	Onshore	32.1/34.8	0.05	5
Beit Dagan	Inland	32.0/34.8	7.5	33
Weizmann	Inland	31.9/34.8	11.5	60
Nevatim	Southern	31.2/34.9	44	400
Hazerim	Southern	31.2/34.7	70	200

950 *Ceilometer Weizmann is a CL51

951
952
953
954
955

Table 3. Ceilometers configurations

Location	Type	Time resolution(sec)	Height resolution (m)	*Height range (km)
Mount Meron	CL31	16	10	7.7
Ramat David	CL31	16	10	7.7
Hadera	CL31	16	10	7.7
Tel Aviv	CL31	16	10	7.7
Beit Dagan	CL31	15	10	7.7
Weizmann	CL51	16	10	15.4
Nevatim	CL31	16	10	7.7
Hazerim	CL31	16	10	7.7

956 * Height range depends on sky conditions and is limited as AOD increases.

957 * In all ceilometers but in Beit Dagan site, data acquisition was limited to 4.5 km based on the BLview firmware

958
959
960
961
962
963
964

Table 4. Ceilometer technical information

Location	Type	Engine board	Receiver	Transmitter	Firmware
Beit Dagan	CL31	CLE311	CLR311	CLT311	1.72
Weizmann	CL51	CLE321	CLRE321	CLT521	1.03

965
966

967
 968
 969
 970
 971
 972
 973
 974
 975
 976
 977
 978
 979
 980
 981
 982
 983
 984
 985
 986
 987
 988

Table 5. Hourly maximum concentration of PM2.5, collected from 21 monitoring sites, between 7-10 September 2015. The values are ranked from low (dark green) to high (dark red) values.

No.	Site	Height (m ASL)	Region	PM2.5 ($\mu\text{g m}^{-3}$)			
				7-Sep-15	8-Sep-15	9-Sep-15	10-Sep-15
1	Kefar Masarik	8	North	52	378	389	378
2	Ahuza	280	North	36	743	650	419
3	Newe Shaanan	240	North	43	400	466	525
4	Nesher	90	North	43	564	496	349
5	Kiryat Biyalic	25	North	53	424	703	447
6	Kiryat Binyamin	5	North	40	223	412	256
7	Kiryat Tivon	201	North	47	413	416	300
8	Afula	57	North	44	836	550	405
9	Raanana	54	Coast	38	173	291	229
10	Antolonsky	34	Coast	32	470	626	386
11	Ashdod	25	Coast	36	303	750	332
12	Ironi D	12	Coast	34	424	507	327
13	Tel aviv Central Station	29	Coast	41	716	803	451
14	Ashkelon	25	Coast	61	182	537	119
15	Jerusalem Efrata	749	Mountain	106	2285	434	403
16	Jerusalem Bar Ilan	770	Mountain	107	3063	641	518
17	Gedera	70	South	34	433	683	308
18	Nir Israel	30	South	25	363	638	228
19	Kiryat Gvaram	95	South	42	376	870	300
20	Sede Yoav	105	South	45	323	245	228
21	Negev Mizrahi	577	South	42	1748	526	317

989

990

991 Table 6. Hourly maximum concentration of PM10, collected from 31 monitoring sites, between 7-10
 992 September 2015. The values are ranked from low (dark green) to high (dark red) values.

No.	Site	Height (m ASL)	Region	PM10 ($\mu\text{g m}^{-3}$)			
				7-Sep-15	8-Sep-15	9-Sep-15	10-Sep-15
1	Galil Maaravi	297	North	114	3130	1987	1562
2	Karmelia	215	North	39	1120	1008	765
3	Newe Shaanan	240	North	104	3459	2471	1518
4	Haifa Port	0	North	78	1600	1965	1699
5	Nesher	90	North	117	3265	2746	1270
6	Kiryat Haim	0	North	82	1161	1625	1088
7	Afula	57	North	97	3239	2322	1961
8	Um El Kotof	0	Coast	99	2025	2028	1630
9	Orot Rabin	0	Coast	58	1152	1455	999
10	Barta	0	Coast	112	2540	2345	1612
11	Qysaria	19	Coast	54	1067	2116	1272
12	Rehuvot	70	Coast	88	2236	3045	1257
13	Givataim	0	Coast	112	1909	4014	1484
14	Yad Avner	77	Coast	61	1738	2902	1252
15	Ameil	20	Coast	96	2027	3472	1321
16	Shikun Lamed	17	Coast	51	1701	3244	1097
17	Station	29	Coast	87	1420	2176	998
18	Ashkelon	29	Coast	117	953	1692	551
19	Ariel	546	Mountain	128	2723	1481	1358
20	Jerusalem Efrata	770	Mountain	273	7820	1630	1437
21	Jerusalem Bar Ilan	749	Mountain	181	5588	1191	966
22	Jerusalem Safra	797	Mountain	491	10280	2389	1780
23	Gush Ezion	960	Mountain	310	6230	1679	1119
24	Erez	80	South	44	1000	1000	718
25	Beit Shemesh	350	South	115	2097	1943	1788
26	Caray Yosef	260	South	85	1047	784	594
27	Modiin	267	South	185	2701	2245	1980
28	Bat Hadar	54	South	65	1342	2563	841
29	Nir Galim	0	South	94	1479	2292	1027
30	Negev Mizrahi	577	South	183	9031	2806	1730
31	Eilat	0	South	275	1867	1592	1684

993